AGU PUBLICATIONS

JGR

Journal of Geophysical Research: Solid Earth

RESEARCH ARTICLE
10.1002/2014JB011501

Key Points:
- Across-isochron crustal thickness variations are observed at two timescales
- Asymmetries in crustal thickness and seafloor morphology between conjugates

Supporting Information:
- Readme

Correspondence to:
J. Lin,
jlin@whoi.edu

Citation:
Wang, T., B. E. Tucholke, and J. Lin (2015), Spatial and temporal variations in crustal production at the Mid-Atlantic Ridge, 25°N–27°30′N and 0–27 Ma, *J. Geophys. Res. Solid Earth*, *120*, 2119–2142, doi:10.1002/2014JB011501.

Received 7 AUG 2014
Accepted 2 MAR 2015
Accepted article online 6 MAR 2015
Published online 21 APR 2015

Spatial and temporal variations in crustal production at the Mid-Atlantic Ridge, 25°N–27°30′N and 0–27 Ma

Tingting Wang[1], Brian E. Tucholke[2], and Jian Lin[1,2,3]

[1]State Key Laboratory of Marine Geology, School of Ocean and Earth Sciences, Tongji University, Shanghai, China, [2]Department of Geology and Geophysics, Woods Hole Oceanographic Institution, Woods Hole, Massachusetts, USA, [3]Key Laboratory of Marginal Sea Geology, Chinese Academy of Sciences, South China Sea Institute of Oceanology, Guangzhou, China

Abstract We use high-resolution multibeam bathymetry, shipboard gravity, side-scan sonar images, and magnetic anomaly data collected on conjugate flanks of the Mid-Atlantic Ridge at 25°N–27°30′N and out to ~27 Ma crust to investigate the crustal evolution of the ridge. Substantial variations in crustal structure and thickness are observed both along and across isochrons. Along isochrons within spreading segments, there are distinct differences in seafloor morphology and gravity-derived crustal thickness between inside and outside corners. Inside corners are associated with shallow depths, thin crust, and enhanced normal faulting while outside corners have greater depths, thicker crust, and more limited faulting. Across-isochrons, systematic variations in crustal thickness are observed at two different timescales, one at ~2–3 Myr and another at >10 Myr, and these are attributed to temporal changes in melt supply at the ridge axis. The shorter-term variations mostly are in-phase between conjugate ridge flanks, although the actual crustal thickness can be significantly different on the two flanks at any given time. We observe no correlation between crustal thickness and spreading rate. Thus, during periods of low melt supply, tectonic extension must increase to accommodate the full plate separation rate. This extension commonly is concentrated in long-lived faults on only one side of the axial valley, resulting in strong across-axis asymmetries in crustal thickness and seafloor morphology. The thin-crust flank has few volcanic features and exhibits elevated, blocky topography with large-offset, often irregular faults, while the conjugate thicker-crust flank shows shorter-offset, regular faulting, and common volcanic features. The variations in melt supply at the ridge axis most likely are caused either by episodic convection in the subaxial mantle or by variable melting of chemically heterogeneous mantle.

1. Introduction

Accretion of oceanic lithosphere is episodic at mid-ocean ridges of all spreading rates, but the frequency of these episodes is lowest at slow-spreading ridges. Alternating episodes of relatively robust magmatic accretion and more amagmatic tectonic extension have been suggested by several lines of evidence at slow-spreading ridges, including variation in off-axis gravity anomalies [*Rommevaux et al.*, 1994; *Tucholke et al.*, 1997; *Maia and Gente*, 1998; *Bonatti et al.*, 2003], changes in fault structure [*Tucholke and Lin*, 1994; *Cannat et al.*, 2006], and changes in crustal composition [*Cannat*, 1993; *Gracia et al.*, 1997; *MacLeod et al.*, 2002; *Bonatti et al.*, 2003]. In addition, crustal structure and seafloor morphology are highly asymmetrical between conjugate ridge flanks along many segments of slow-spreading ridges [e.g., *Shaw*, 1992; *Shaw and Lin*, 1993; *Tucholke and Lin*, 1994; *Cannat et al.*, 1995; *Escartin and Lin*, 1995]. Much of this has been attributed to asymmetric tectonic extension by long-lived detachment faults wherein one ridge flank is emplaced largely by tectonic extension and the other forms by mostly magmatic accretion [*Tucholke and Lin*, 1994; *Tucholke et al.*, 1996a, 1998; *Cann et al.*, 1997; *Fujiwara et al.*, 2003; *Escartin et al.*, 2008]. These factors profoundly affect lithospheric structure and seafloor morphology.

During recent decades, our understanding of ridge-axis processes on slow-spreading ridges has been significantly enhanced by detailed multibeam bathymetric and geophysical surveys [e.g., *Kuo and Forsyth*, 1988; *Lin et al.*, 1990; *Sloan and Patriat*, 1992; *Sempere et al.*, 1993, 1995; *Rommevaux et al.*, 1994; *Gente et al.*, 1995; *Pariso et al.*, 1995; *Searle et al.*, 1998; *Allerton et al.*, 2000; *Sloan and Patriat*, 2004a, 2004b]. However, most of these studies have been limited to crustal ages less than 10 Ma. One exception is mapping that extends to ~26 Ma on the flanks of the Southwest Indian Ridge [*Cannat et al.*, 2006]. Another is on the Mid-Atlantic Ridge (MAR) at ~26°N where surveys extend to ~27 Ma on both ridge flanks (Figure 1). Data from the initial survey in this area were used to analyze

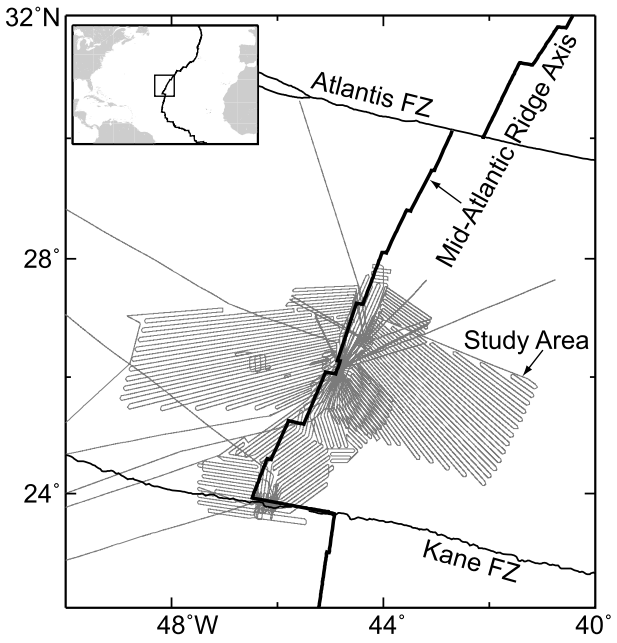

Figure 1. Location of the study area on the Mid-Atlantic Ridge. Ship tracks of the ARSRP [*Tucholke et al.*, 1997], MAREAST [*Tucholke et al.*, 1996b], MODE94 [*Fujimoto et al.*, 1996], and MODE98 [*Fujioka et al.*, 1999] surveys are shown by thin solid lines. The MAR axis is marked by a thick line, and traces of the Atlantis and Kane fracture zones are indicated.

ridge segmentation and crustal structure on the west flank of the MAR [e.g., *Tucholke et al.*, 1997; *Escartin and Lin*, 1998]. A subsequent east flank survey [*Tucholke et al.*, 1996b] provides data needed to consider questions that were not previously addressed, such as total crustal production and symmetry or asymmetry of crustal accretion across the MAR axis. In this study, we use high-resolution multibeam bathymetry, side-scan sonar images, shipboard gravity, and magnetic anomaly data from both ridge flanks to quantify temporal variability in crustal production and to analyze its relationship to tectonic processes at the ridge axis.

2. Data Acquisition and Processing

2.1. Bathymetry

Multibeam bathymetric data used in this study (Figure 2a) were collected during four research cruises. The primary survey on the west flank of the MAR, which extends off axis to 27–28 Ma crust, was conducted during the Office of Naval Research Acoustic Reverberation Special Research Program (ARSRP) in 1992 [*Tucholke et al.*, 1997]. Conjugate east flank data reaching off axis to ~27 Ma crust were obtained during the MAREAST survey in 1996 [*Tucholke et al.*, 1996b]. Track spacing in both surveys was designed to give complete multibeam bathymetric coverage, and it therefore varied from about 4 to 9 km, depending on seafloor depth (Figure 1). Additional data from surveys extending off axis to 5–10 Ma crust were acquired during the MODE98 cruise in the northern part of the study area [*Fujioka et al.*, 1999] and the MODE94 cruise in the south [*Fujimoto et al.*, 1996]. We merged all four data sets to produce a single bathymetric grid (100 m cells) from 24°N to 27°30′N.

2.2. Sediment Thickness

Detailed sediment thickness data are available only for the west flank ARSRP survey [*Jaroslow*, 1996]. In general, average sediment cover thickens with increasing crustal age to ~40 m over 12–19 Ma crust but then thins to ~25 m over 20–28 Ma crust. However, sediment ponds in nontransform discontinuities (NTDs) between spreading segments can contain several hundred meters of sediment and, in exceptional instances, have sediments $>$700 m thick. Local ponds between abyssal hills in the interiors of spreading segments also can have sediment thicknesses of 200 m or more, particularly over 12–19 Ma crust. Because no detailed information on sediment thickness is available outside the west flank survey area, we were unable to systematically account for sediment cover in our gravity and crustal thickness calculations. The effect of this limitation is discussed in sections 2.5 and 2.6.

2.3. Side-Scan Sonar Data

The long-range (~8–10 km) HMR1 side-scan sonar system [*Rognstad*, 1992] was used during the ARSRP and MAREAST surveys. It provided sonar images that completely insonify the seafloor in two look directions orthogonal to ship tracks (Figure 1), thus allowing seafloor features facing both toward and away from the MAR axis to be highlighted. Practical resolution of fine-scale volcanic and tectonic features observed in these images is on the order of 200 m.

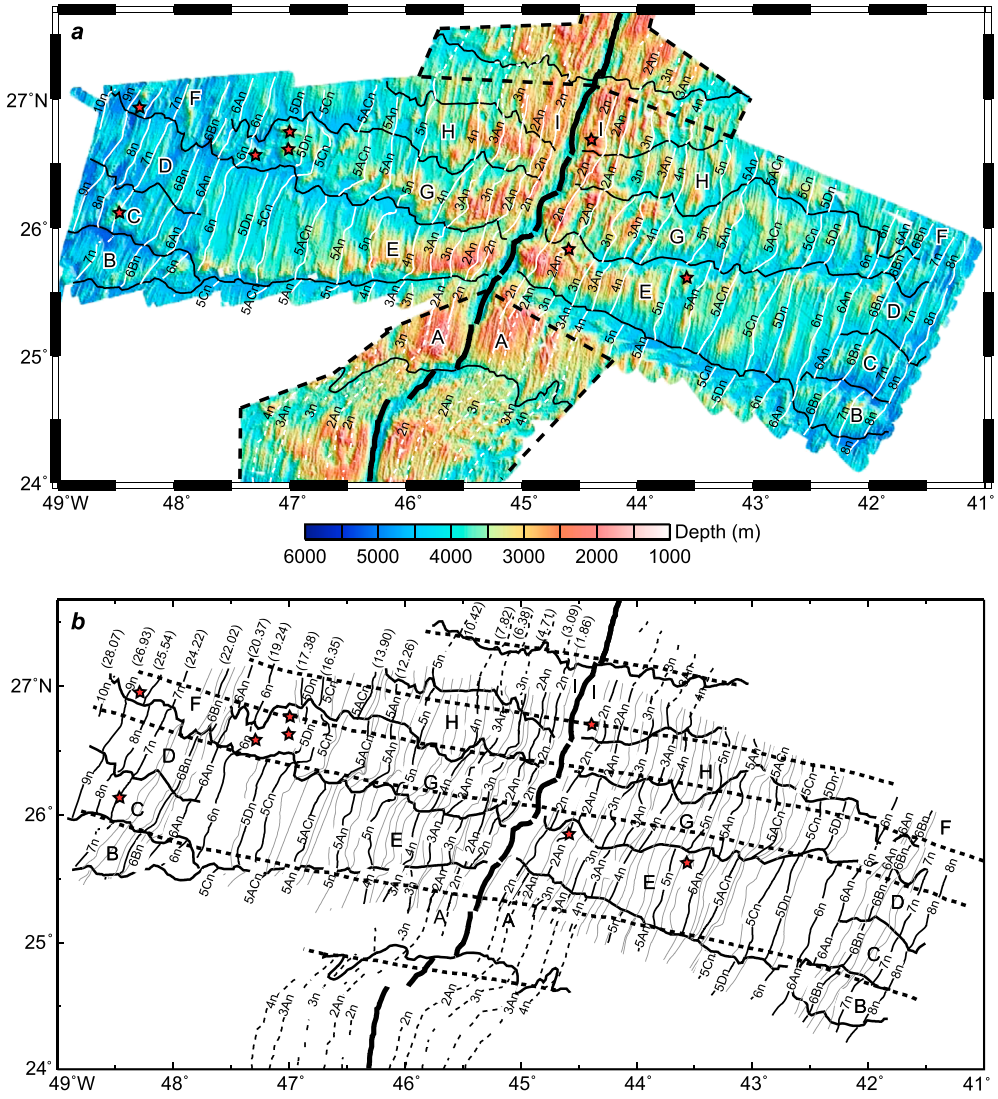

Figure 2. (a) Shaded-relief multibeam bathymetry of the study area. The main west and east flank data were acquired in the ARSRP [*Tucholke et al.*, 1997] and MAREAST [*Tucholke et al.*, 1996b] surveys, respectively. Data from the MODE98 [*Fujioka et al.*, 1999] and MODE94 [*Fujimoto et al.*, 1996] surveys are within the dashed boxes to the north and south, respectively. Thin white lines locate identified magnetic anomalies [*Tucholke et al.*, 1996b; *Tivey et al.*, 1998; *Tivey and Tucholke*, 1998; *Fujioka et al.*, 1999]. The MAR axis and traces of nontransform discontinuities (NTDs), shown as thick and medium black lines, respectively, are identified from seafloor morphology and magnetic anomaly offsets. Stars show locations of megamullions [*Tucholke et al.*, 1996a, 1998]. Letters A–I mark the nine spreading segments analyzed in the present study. (b) Detail of magnetic anomalies within the study area; ages of major chrons (Ma, in parentheses) are based on *Ogg* [2012]. Heavy dashed lines show flow lines of relative plate motion [*Klitgord and Schouten*, 1986] over the past 28 Myr.

2.4. Magnetic Anomalies and Crustal Ages

Magnetic anomalies (Figure 2b) on the two ridge flanks were interpreted from surface-towed magnetometer data obtained in the ARSRP and MAREAST surveys [*Tucholke et al.*, 1996b, 1997; *Tivey and Tucholke*, 1998]. Magnetic anomaly interpretations north of 27°N [*Fujioka et al.*, 1999] and at 24°N–25°N [*Tivey et al.*, 1998] (light dashed lines in Figure 2b) were incorporated to produce a data set that covers the entire study area. Crustal ages assigned to the identified magnetic anomalies are based on the geomagnetic polarity timescale of *Ogg* [2012].

2.5. Gravity

Free-air gravity data were compiled from shipboard gravity measurements of the four surveys [*Fujimoto et al.*, 1996; *Tucholke et al.*, 1996b, 1997; *Fujioka et al.*, 1999], in which track line spacing varied from ~4 to 9 km.

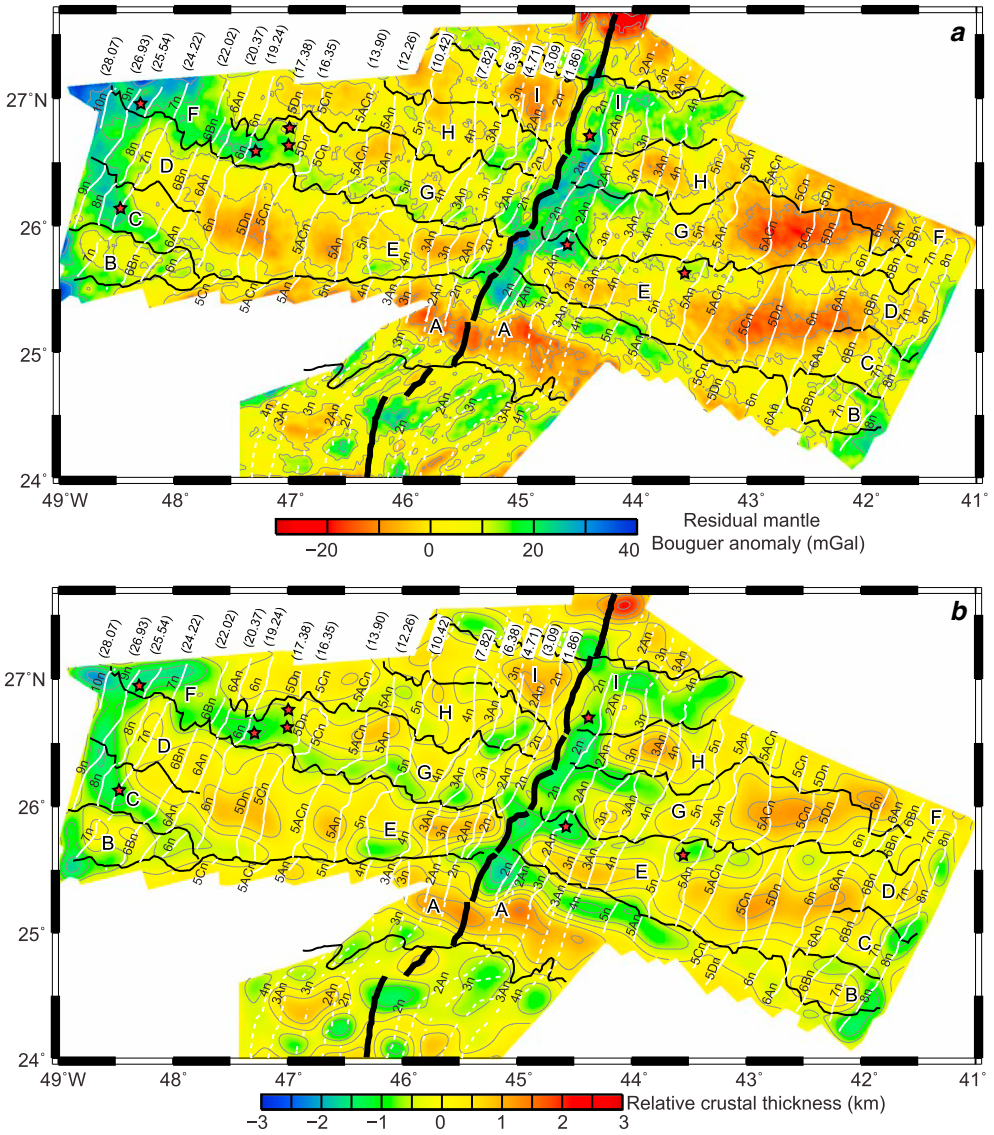

Figure 3. (a) Map of residual mantle Bouguer anomaly (RMBA), calculated using parameters discussed in text. Labeling as in Figure 2. Contour interval is 10 mGal. (b) Map of crustal thickness variations relative to a 6 km model reference thickness. Labeling as in Figure 2. Contour interval is 0.5 km.

The crossover misfits between gravity measurements along track lines have root-mean-square (RMS) values of 1–2 mGal for the ARSRP and MAREAST surveys and slightly larger RMS values (generally <4 mGal) for gravity data sets merged from the other surveys. We subtracted the gravitational effects of seafloor topography and relief on the crust-mantle interface from the free-air gravity anomaly to obtain mantle Bouguer anomalies (MBAs), assuming a reference crustal thickness of 6 km and using the spectrum method of *Parker* [1972]. Densities of water, crust, and mantle were assumed to be 1.03, 2.7, and 3.3×10^3 kg m^{-3}, respectively.

Residual mantle Bouguer anomalies (RMBAs; Figure 3a) were calculated by removing from MBA the gravitational effect of lithospheric cooling, based on a 3-D mantle thermal model. The mantle thermal structure was calculated for a 100 km thick layer, using the 2-D age grid (Figure 2b) and assuming simple 1-D plate cooling [*Turcotte and Schubert*, 2002; *Wang et al*., 2011]. The parameters used in the calculation are the same as in *Wang et al*. [2011]. This mantle thermal model was then converted to a 3-D mantle density structure, which was used to calculate gravitational effects. Within a narrow axial region that contains ridge-axis offsets, this 1-D plate cooling model differs slightly from the 3-D passive mantle upwelling model used in *Tucholke et al*. [1997], in which lateral heat transfer across ridge offsets was considered. Thus, for the 3-D

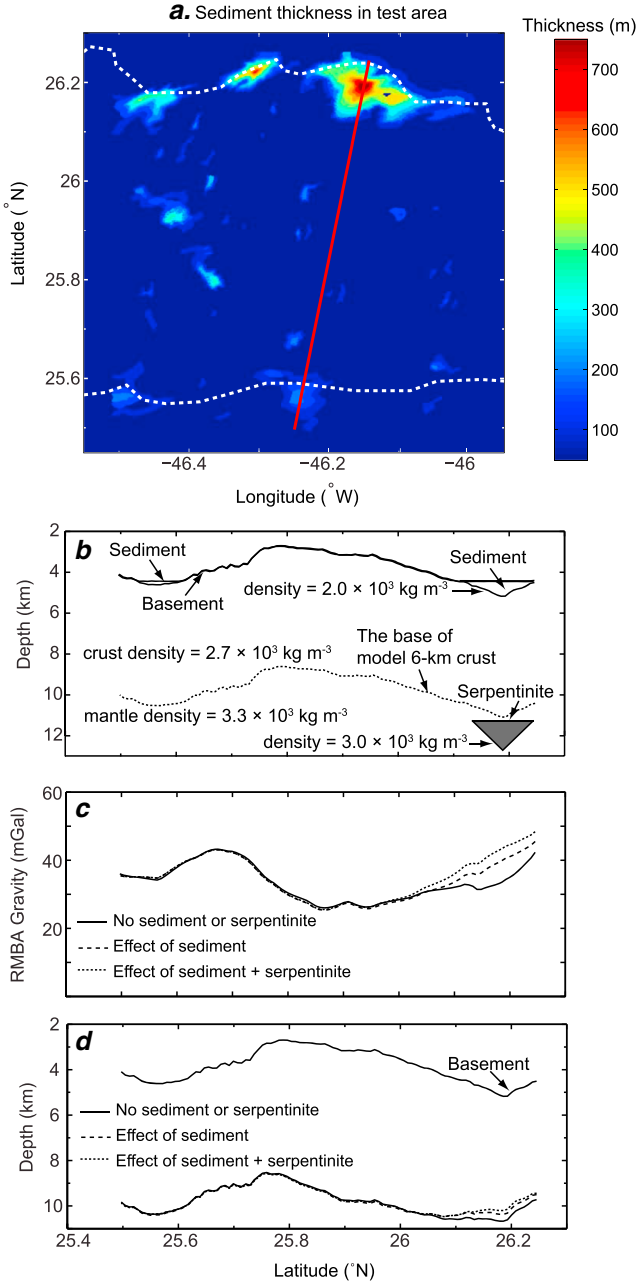

Figure 4. Effect of sediment thickness, and the possible presence of serpentinite, on calculated RMBA and modeled crustal thickness. (a) Map of sediment thickness within part of the ARSRP survey on the west flank of the MAR. Dotted lines show the axes of NTDs. The red line passes through the thickest sediment in the ARSRP survey area, in the northern NTD. (b) Model along the profile in Figure 4a, showing observed basement depth and sediment thickness, as well as a hypothetical serpentinite body beneath the sediment pond in the northern NTD. The dotted line shows the base of reference 6 km thick crust. The serpentinite body has a top diameter of 13 km and a thickness of 2 km and is located 11 to 13 km below sea level. (c) Effect of sediment thickness and the hypothetical serpentinite body on RBMA. Accounting for the sediment in the area of maximum sediment thickness (~750 m) increases the RMBA by about 6 mGal, and accounting for the hypothetical serpentinite body increases the RMBA by about 3.5 mGal. (d) Effect of sediment thickness and the hypothetical serpentinite body on model crustal thickness. Properly accounting for sediment cover decreases model crustal thickness by about 0.3 km in the area of thickest sediment, and accounting for the hypothetical serpentinite decreases model crustal thickness by about 0.1 km. The magnitude and extent of the serpentinite effect are highly dependent on the density, size, depth, and configuration of the serpentinite body.

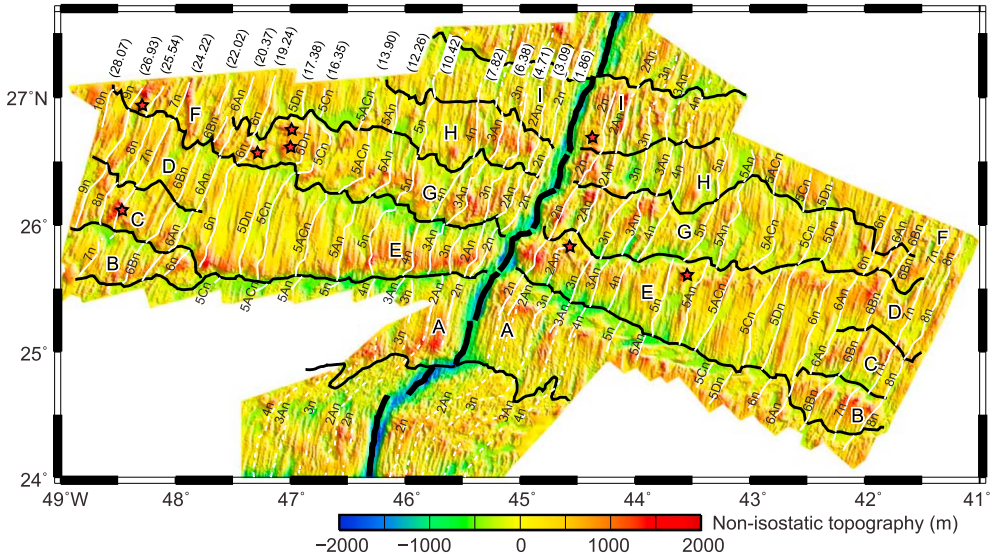

Figure 5. Map of nonisostatic topography. Labeling as in Figure 2. IC crust (generally at north edges of segments on east flank, south edges on west flank) stands out as being out of isostatic equilibrium, and it probably is stress supported.

passive upwelling model, the calculated thermal structure and resultant gravity corrections are smoother across ridge offsets than those predicted by the 1-D plate cooling model. However, differences between the two models are only a few mGals and are limited to a narrow zone proportional to the size of ridge offsets.

Our calculations assumed that crust with density 2.7×10^3 kg m^{-3} was present immediately below the seafloor at all locations, but as we noted earlier, there are locally substantial thicknesses of sediment, most notably in NTDs. We tested the effect of sediment thickness on gravity calculations along a profile that included the maximum observed sediment thickness (~750 m) within the ARSRP survey area (Figures 4a and 4b). In the area of maximum sediment thickness, the calculated RMBA is increased by about 6 mGal if the gravitational effect of the sediment is considered (Figure 4c).

Along slow-spreading ridges, normal faulting commonly facilitates penetration of seawater to the upper mantle, leading to serpentinization and emplacement of peridotites at or near the seafloor [e.g., *Tucholke and Lin*, 1994; *Cannat et al*., 1995]. Such occurrences almost certainly are present within our study area, primarily where crustal thickness is reduced and normal faults therefore can more readily reach the mantle. These areas are dominantly at segment ends and in the adjacent NTDs. Serpentinized mantle has reduced density that can be as low as that of ocean crust [e.g., *Escartin et al*., 2001], so areas of reduced crustal thickness may contain substantial volumes of serpentinized mantle rocks that can affect gravity and crustal thickness calculations. We tested the gravitational effect of possible partial serpentinization using a simple model of reduced mantle density (3.0×10^3 kg m^{-3}) beneath a NTD as shown in Figure 4b. Accounting for the modeled serpentinization would increase the RMBA by about 3.5 mGal. The magnitude and extent of the effect of course depend on the density, size, depth, and configuration of the serpentinite body. However, the important point is that accounting for possible serpentinite will result in more positive local RMBA values.

2.6. Crustal Thickness

Relative crustal thickness variations (Figure 3b) were calculated by downward continuation of RMBA to the base of a model 6 km thick crust with a crust/mantle density contrast of 0.6×10^3 kg m^{-3} (e.g., 3.3–2.7×10^3 kg m^{-3}) [*Kuo and Forsyth*, 1988; *Lin et al*., 1990]. This is an end-member model that assumes that the RMBA signal is caused only by crustal thickness variations. Calculated crustal thicknesses vary up to about ±2 km from the model reference thickness of 6 km, and they show a Gaussian distribution (see Figure S1 in the supporting information).

The effect of sediment thickness on calculated crustal thickness is shown in Figure 4d. In the area of the greatest observed sediment thickness (~750 m), properly accounting for the sediment cover would locally decrease model crustal thickness by about 0.3 km. Because most areas of thick sediments are in NTDs, it is

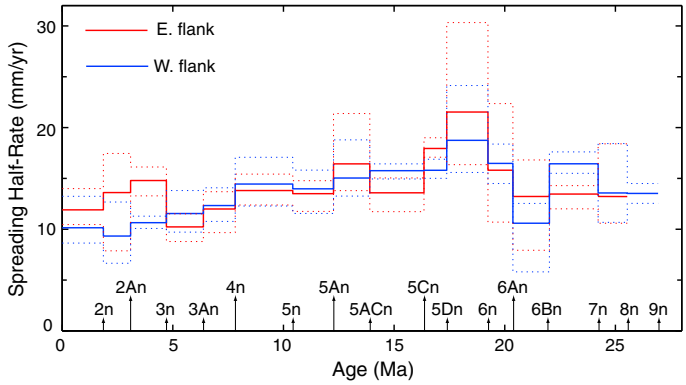

Figure 6. Average spreading half rates versus time for the west (blue solid line) and east (red solid line) flanks of the MAR in our study area. Rates on each flank were calculated for individual segments and then averaged. Red and blue dotted lines show the range of variation for all segments on each flank.

likely that actual crustal thickness in NTDs is less than modeled thickness throughout the survey area, but particularly on older crust beneath sediment ponds.

The effect that serpentinization may have on calculated crustal thickness is also shown in Figure 4d. Like the case for sediments, accounting for serpentinization would locally decrease the calculated crustal thickness. Serpentinized peridotites, if present, are likely to occur in NTDs and other zones of thin crust

Table 1. Spreading Half-Rate (mm yr^{-1}) of Individual Segments

Anomaly	Age (Ma)	SegA	SegE	SegG	SegH	SegI	SegB	SegC	SegD
				MAR West Flank					
0-2n	0–1.86	13.23	10.63	8.64	8.99	9.24	—	—	—
2n-2An	1.86–3.09	12.68	6.65	9.03	9.40	8.89	—	—	—
2An-3n	3.09–4.71	10.62	11.28	10.96	10.07	10.26	—	—	—
3n-3An	4.71–6.38	12.00	10.29	11.91	9.71	13.80	—	—	—
3An-4n	6.38–7.82	14.08	12.01	10.76	13.70	11.07	—	—	—
4n-5n	7.82–10.42	12.28	13.78	13.89	17.07	15.18	—	—	—
5n-5An	10.42–12.26	15.81	13.47	11.55	14.65	14.39	—	—	—
5An-5ACn	12.26–13.90	13.26	18.79	13.38	14.72	—	—	—	—
5Acn-5Cn	13.90–16.35	15.58	14.95	16.43	16.07	—	—	—	—
5Cn-5Dn	16.35–17.38	—	15.50	15.00	16.88	—	—	—	—
5Dn-6n	17.38–19.24	—	16.52	24.14	15.58	—	—	—	—
6n-6An	19.24–20.37	—	17.42	18.37	16.56	—	14.50	—	—
6An-6Bn	20.37–22.02	—	—	5.81	11.60	—	10.86	12.53	12.14
6Bn-7n	22.02–24.22	—	—	—	—	—	15.49	17.60	16.21
7n-8n	24.22–25.54	—	—	—	—	—	18.43	11.61	10.67
8n-9n	25.54–26.93	—	—	—	—	—	—	12.54	14.50
				MAR East Flank					
0-2n	0–1.86	11.14	12.35	10.46	11.59	14.00	—	—	—
2n-2An	1.86–3.09	7.87	14.77	17.45	15.97	11.98	—	—	—
2An-3n	3.09–4.71	13.28	15.94	15.02	16.12	13.58	—	—	—
3n-3An	4.71–6.38	11.51	9.49	10.29	11.06	8.79	—	—	—
3An-4n	6.38–7.82	10.85	12.54	13.22	9.67	13.69	—	—	—
4n-5n	7.82–10.42	13.21	15.42	14.72	13.29	12.38	—	—	—
5n-5An	10.42–12.26	14.78	14.20	11.75	13.26	—	—	—	—
5An-5ACn	12.26–13.90	—	13.80	21.38	14.11	—	—	—	—
5Acn-5Cn	13.90–16.35	—	15.04	13.96	11.73	—	—	—	—
5Cn-5Dn	16.35–17.38	19.00	17.32	17.08	18.37	—	—	—	—
5Dn-6n	17.38–19.24	18.23	16.35	21.20	30.33	—	—	—	—
6n-6An	19.24–20.37	22.36	15.52	10.69	14.35	—	—	—	—
6An-6Bn	20.37–22.02	16.81	—	7.93	8.77	—	15.24	14.45	16.11
6Bn-7n	22.02–24.22	13.82	—	—	—	—	12.00	14.29	14.08
7n-8n	24.22–25.54	10.88	—	—	—	—	18.39	10.59	12.59

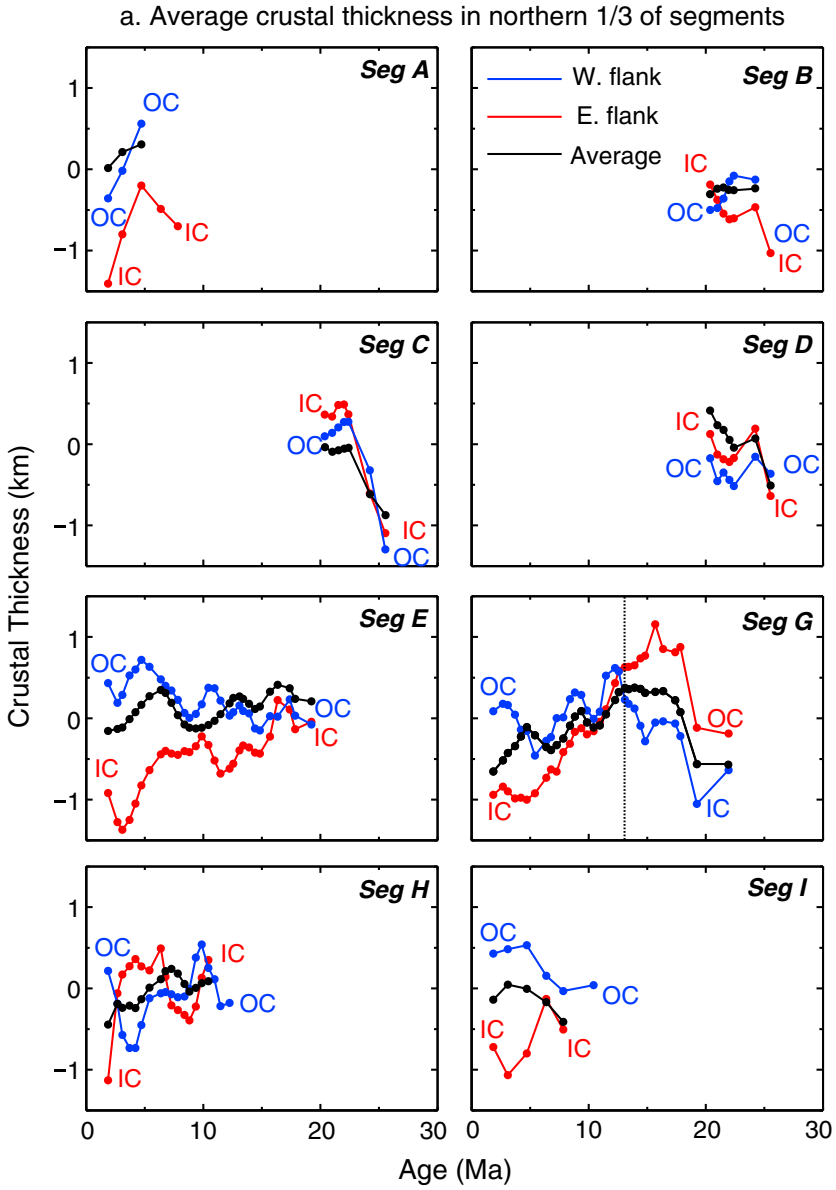

Figure 7. Average crustal thickness (relative to 6-km model reference thickness) versus time within the (a) northern, (b) central, and (c) southern one thirds of spreading segments in the study area. Averages are as defined in the text. The average of each whole segment (black line, data from Figure 9a) incorporates data from both ridge flanks. In Figure 7a, note the reversal of IC and OC positions in the northern one third of segment G crust older than about 13 Ma; this is due to reversal of offset in the NTD bounding the northern edge of this segment (see Figure 2). In Figures 7a and 7c, note that with rare exceptions, IC crust is thinner than OC crust.

within segments. Considering the possible serpentinization effect as well as sediment ponding, actual crustal thickness differences between segment centers and segment ends/NTDs are probably greater than indicated by the model calculations. More generally, the possibility of serpentinization in any zone of thin crust suggests that the modeled crustal thickness variations (Figure 3b) represent minimum variations in actual igneous crustal thickness.

2.7. Nonisostatic Topography

We define nonisostatic topography (Figure 5) as the observed seafloor topography minus the predicted effects of plate cooling and the isostatically compensated topography. The nonisostatic topography thus can reveal topographic features that are supported by lithospheric stresses. The predicted effect of plate cooling is

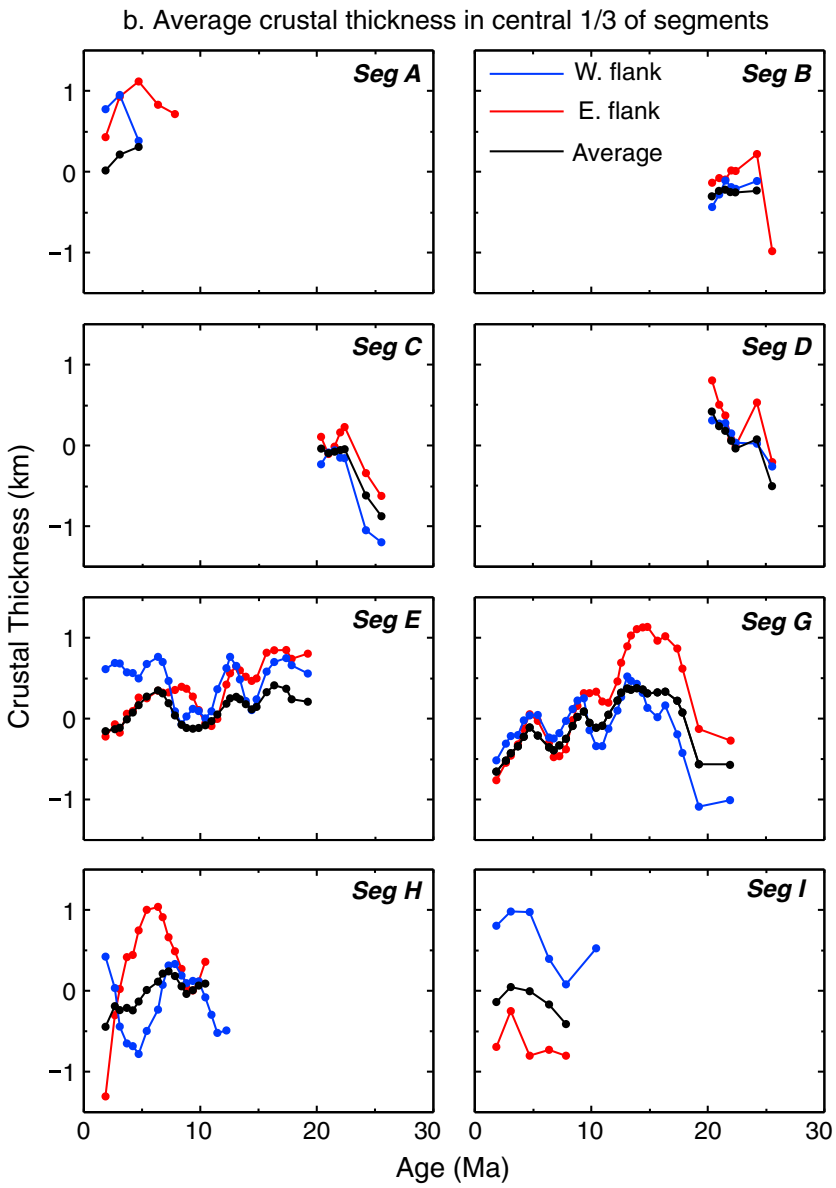

Figure 7. (continued)

calculated using the same plate cooling model and the same parameters as for the RMBA calculation [*Wang et al.*, 2011]. The isostatic topography, Z_{iso}, is calculated as $Z_{iso} = \Delta h \times (\rho_m - \rho_c)/(\rho_m - \rho_w)$, assuming Airy compensation, where Δh is crustal thickness and ρ_m, ρ_c, and ρ_w are densities of mantle, crust, and water, respectively, as noted in section 2.5.

3. Derived Parameters

3.1. Bathymetric Relief Along Isochrons

Seafloor depth relief along the MAR axis within individual spreading segments has been suggested as an indicator of magmatic robustness of the segments [e.g., *Lin et al.*, 1990]. To help infer the level of magmatism in spreading segments through time, we calculated maximum depth relief, ΔD, along the magnetic anomaly isochrons within the segments shown in Figure 2b (average sample interval <1 Myr over the run of the segments, i.e., along plate flow lines). For each isochron, we determined the minimum depth within the central one third of the segment, averaged for the two ridge flanks. The position of these picks takes into account the

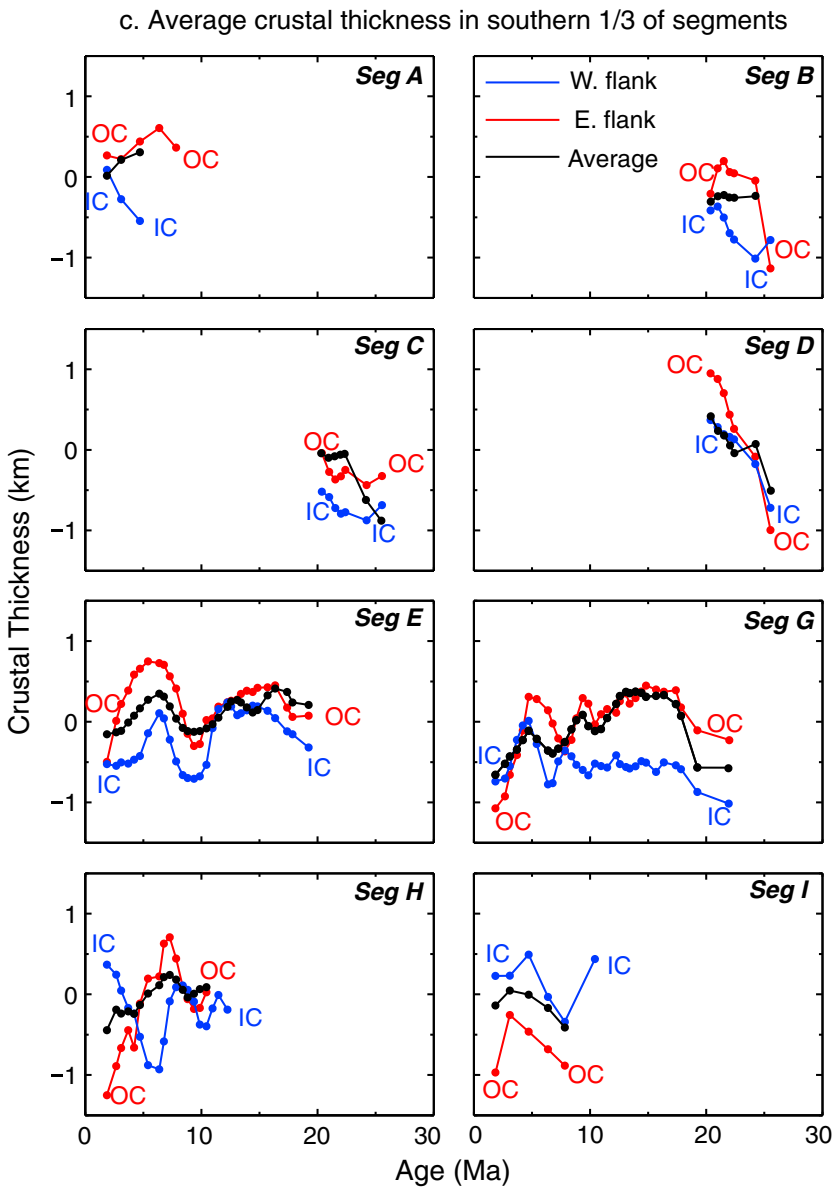

Figure 7. (continued)

fact that segment midpoints are most representative of magma input [*Lin et al.*, 1990; *Gente et al.*, 1995] and it discounts depths at inside corners of spreading segments, which in places can be tectonically uplifted to depths shallower than those at segment centers. Maximum depth was calculated as the average of the four maximum depths in the NTDs at the segment ends of pairs of conjugate isochrons on the ridge flanks.

3.2. Gravity Variation Along Isochrons

Like depth relief, along-isochron variation in gravity has been used to infer magmatic robustness within spreading segments [e.g., *Lin et al.*, 1990; *Gente et al.*, 1995]. We calculated ΔRMBA along isochrons within each spreading segment, picking the RMBA values at the same locations as those used to calculate ΔD and averaging them in the same way.

3.3. Spreading Rates

Spreading rates between major isochrons were calculated for the east and west flanks of each ridge segment within the study area (Figure 6 and Table 1). Average half rates for the entire survey area have steadily

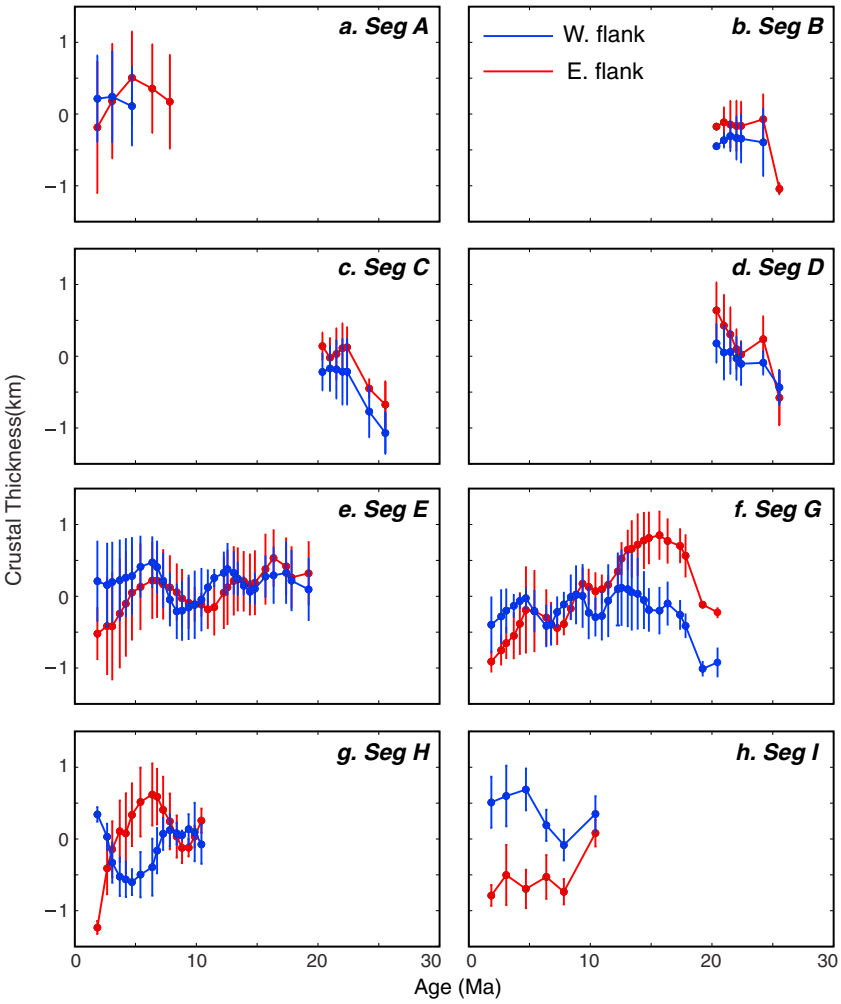

Figure 8. Average crustal thickness versus time for conjugate ridge flanks in individual spreading segments. West flank data are shown in blue and east flank data are shown in red. Bars show standard deviations. Crustal thickness for each data point is an along-isochron average value as defined in the text. Note that most crustal thickness variations are in-phase between conjugate ridge flanks, although actual thicknesses in conjugates may differ at any point in time. Thickness variations in segment H are almost directly antiphase.

decreased since ~19 Ma, from rates as high as ~20 mm yr^{-1} to only 10–12 mm yr^{-1} in the past 2 Myr. Prior to ~19 Ma, average half rates were about 13–16 mm yr^{-1}. Calculated half rates within individual spreading segments, however, deviate significantly from these averages, ranging between 30 and 6 mm yr^{-1} (Table 1). Seafloor spreading commonly has been asymmetrical, most notably at ages <5 Ma and ~14–24 Ma (Figure 6). For the entire survey area, average spreading asymmetry has been <4 mm yr^{-1}. Within individual segments, asymmetries generally are less than 5 mm yr^{-1} but in some places they exceed 10 mm yr^{-1} (e.g., Segment H at 5Dn-6n; Table 1). Polarity of the spreading asymmetries has alternated randomly between the two ridge flanks over time.

3.4. Temporal Variations in Crustal Thickness

In order to assess temporal variations in crustal thickness quantitatively, we sampled the spreading segments at the magnetic anomaly isochrons shown in Figure 2b to provide crustal thickness data at an average interval of <1 Myr over the run of the segments. We combined these values in several ways. First, we divided each segment into northern, central, and southern one thirds in order to compare crustal thicknesses between inside corners (ICs), segment centers, and outside corners (OCs); within these one thirds, we derived average crustal thickness along each isochron on each ridge flank (Figure 7). These values were then combined along

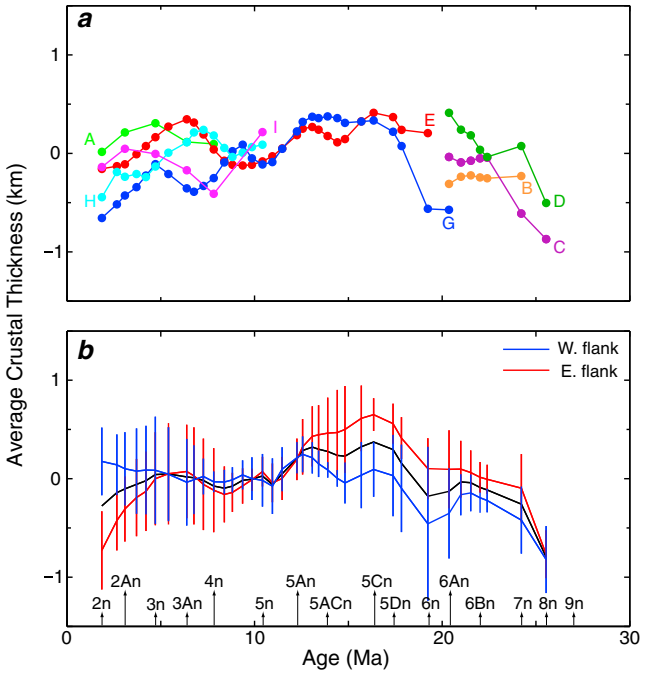

Figure 9. (a) Crustal thickness (average of conjugate ridge flanks) versus age for individual ridge segments, as labeled, in the study area. Averages are as defined in the text. Note that variations in crustal thickness are largely independent from one segment to another for most time intervals. (b) Average crustal thickness (black line) within the study area for all segments combined, versus crustal age. Averages are as defined in the text. Separate west flank data (blue) and east flank data (red) are also shown. Bars show standard deviations. Note the long-term trends of increasing average thickness from ~25 to 17 Ma and decreasing thickness since ~13 Ma.

each isochron to provide average crustal thickness on each flank of each segment through time (Figure 8). To compare crustal thickness variations between individual full spreading segments through time, we averaged the data for conjugate isochrons within each segment on the two ridge flanks (Figure 9a); these full-segment averages are also shown in Figure 7 for comparison with IC, segment center, and OC values. Finally, the crustal thicknesses at each isochron were averaged together for all segments to provide a perspective on regional melt production through time (Figure 9b).

4. Characteristics of Ridge Segmentation

The combined survey data were used to examine nine spreading segments in the study area. *Tucholke et al.* [1997] described the detailed evolution of the spreading segments on the west flank; the observed segmentation on the conjugate east flank is consistent with the west flank pattern. Off-axis traces of the NTDs are identified from both seafloor morphology and magnetic anomaly offsets (Figure 2). The NTDs are irregular and deviate significantly from flow lines of relative plate motion as spreading segments have lengthened and shortened through time (Figure 2b). Some ridge segments have terminated, either by consolidation of adjacent segments (e.g., segments C and D) or by being cut off by propagation of an adjacent NTD (e.g., segment B).

With few exceptions, the spreading segments are separated by right-stepping NTDs that have offset the ridge axis by 0 to 58 km (average ~30 km) over the past ~28 Myr [*Tucholke et al.*, 1997] (Figure 2). Where the right-stepping offsets occur, IC crust lies at the northern edges of spreading segments on the east flank of the MAR, and OC crust is at the northern edges on the west flank; this is reversed at the southern edges of the segments. The only significant departure from right-stepping offsets at the NTDs occurs on the northern side of segment G in crust between anomalies 5An and 6n (~13–19 Ma). In that location, the NTD is a left-stepping offset and the northern part of the segment, like the southern part, is IC crust (Figure 2). Elsewhere, there are minor, temporary left-stepping offsets or, more commonly, zero offsets such as those in younger crust along the southern margin of segment I (Figure 2). None of these deviations have significantly affected the continuity of the observed ridge-flank segmentation [*Tucholke et al.*, 1997], although they do locally affect variations in crustal structure that are typically associated with ICs and OCs.

Megamullions (oceanic core complexes that have domed shapes and prominent corrugations) that have formed by long-lived detachment faulting occur at several locations in the study area (Figures 2, 3, and 5, stars) [*Tucholke et al.*, 1996a, 1998]. One set of these is in the west flank of segment G at ~17–19 Ma, in the region where this segment is bounded to the north and south by inside corners (Figure S9). Another prominent example is Dante's Domes in the southern part of segment I just east of the MAR axis (see Figure 12) [*Tucholke et al.*, 2001]. Two well-developed megamullions also appear in segments C and F on the west

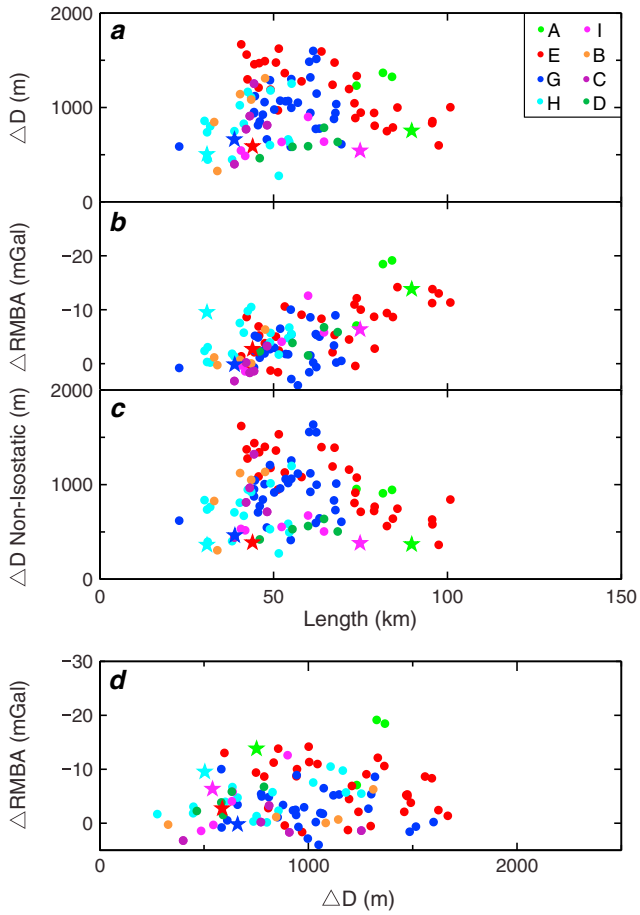

Figure 10. Relationships between ΔD, ΔRMBA, ΔD nonisostatic, and segment length. ΔD and ΔRMBA are along-isochron variation of seafloor depth and RMBA within a given segment as defined in the text. Data from different segments are shown by different colors. (a) ΔD versus segment length; (b) ΔRMBA versus segment length; (c) ΔD nonisostatic versus segment length; and (d) ΔRMBA versus ΔD. Stars show values at the ridge axis.

flank of the MAR, and less developed examples appear in the northern, IC crust along the east flank of segment E (Figures 2, 3, and 5).

Comparisons of segment length, ΔD, and ΔRMBA, sampled at an average interval of <1 Myr over the run of the spreading segments, are shown in Figure 10. Segment lengths have ranged from about 20 to 100 km and averaged 50–60 km (Figures 10a–10c). ΔD values are mostly between 500 m and 1500 m and average ~1000 m (Figure 10a). Unlike the positive correlation between ΔD and segment length suggested by *Lin et al*. [1990] for a larger, on-axis MAR data set, the few samples of axial values (Figure 10a, stars) do not show strong variations, and the off-axis values show no clear correlation.

ΔRMBA has varied widely from slightly negative to ~20 mGal and averages ~5 mGal (Figure 10b). Unlike ΔD, ΔRMBA shows a trend of increasing values with increasing segment length, although there is significant scatter. This pattern appears in both axial data (Figure 10b, stars) and off-axis data. The apparent trend of increasing ΔRMBA with increasing segment length suggests that longer ridge segments are associated with greater relative values of crustal thickness near segment midpoints, which is consistent with the finding of *Lin et al*. [1990] based on an on-axis MAR data set. In contrast, the lack of such correlation between ΔD and segment length may indicate that seafloor topography, and thus ΔD, reflects not only isostatic response to crustal thickness variations but also other nonisostatic components supported by lithospheric stresses. This is consistent with the plot in Figure 10c, where nonisostatic components of the topography show no obvious relationship with ridge segment length. As might be expected from the separate plots of ΔD and ΔRMBA versus segment length, these parameters show no correlation when plotted against one another (Figure 10d).

5. Segment-Scale Variations

5.1. Along Isochrons

There is clear along-isochron asymmetry of crustal thickness within individual spreading segments. Overall, segment centers exhibit thick crust compared to segment ends (Figure 3b). At segment ends, however, ICs generally have thin crust while OCs have thicker crust (Figures 7a and 7c). Moreover, ICs are at shallow depths (Figure 2a) and stand out as elevated features on the map of nonisostatic topography (Figure 5). In contrast, OCs are at normal depths and are close to being isostatically compensated. Differences in crustal thickness of conjugate IC/OC crustal parcels can exceed 1 km (Figures 7a and 7c), and differences in depth can reach up to 2 km.

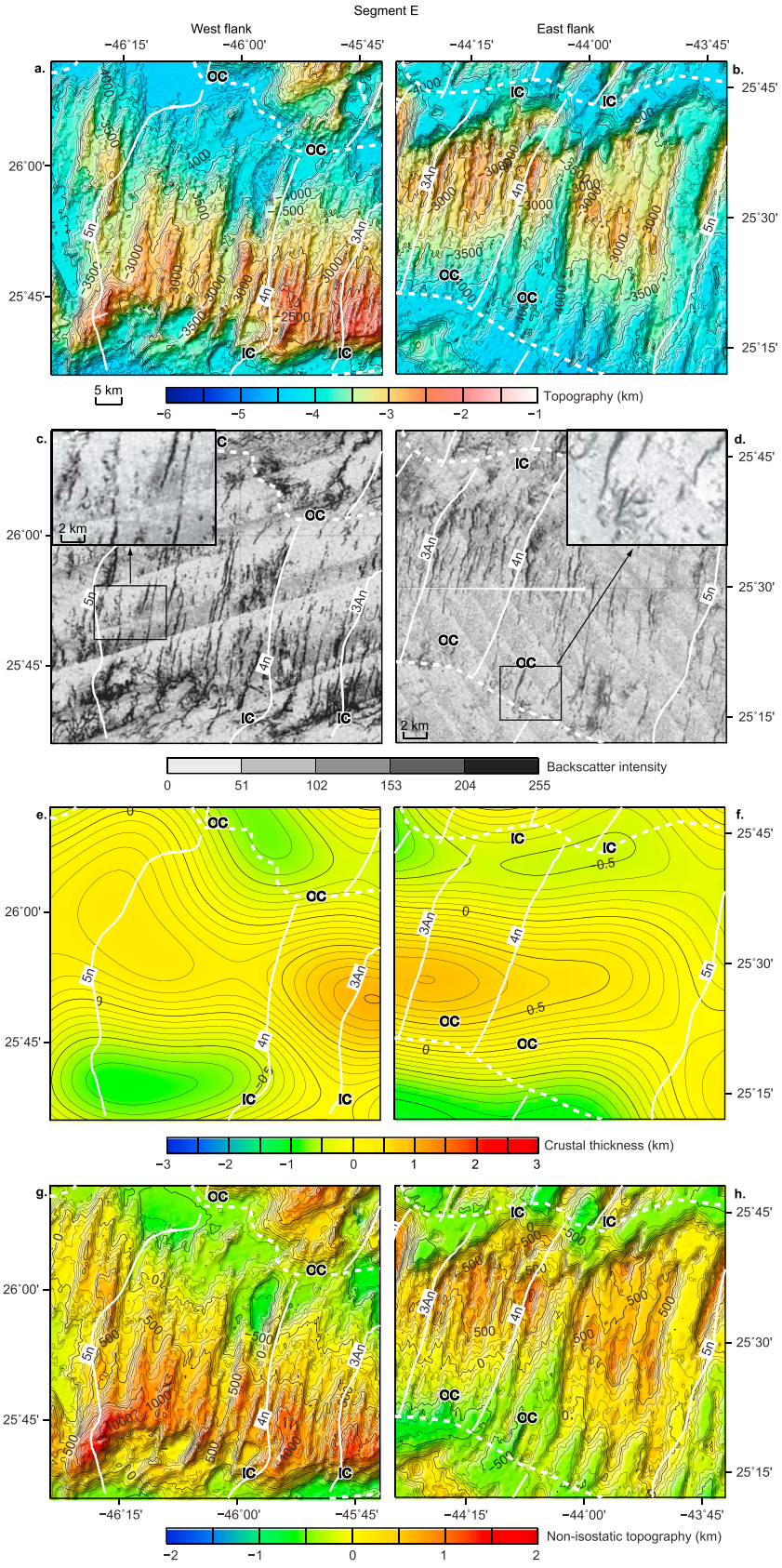

Figure 11

5.2. Across-Isochron, Temporal Variations

Across-isochron changes in crustal thickness are present on both flanks of the ridge axis, with crust thickening and thinning at timescales of ~2–3 Myr (Figures 7 and 8). Peak-to-trough amplitudes of these changes along the run of IC, OC, and center positions of segments can exceed 1 km (Figure 7). These variations are also reflected in average crustal thickness (Figure 8) although they are somewhat damped. Crustal thickness variations are in-phase or nearly in-phase between conjugates in most spreading segments (Figure 8), with the notable exception of segment H. In that segment, crustal thickness changes are close to being directly antiphase (Figure 8g).

5.3. Crustal Thickness Comparisons Between Conjugates

Superimposed on the general phase symmetry of crustal thickness variations, actual crustal thicknesses between conjugate flanks can be nearly the same (symmetrical) or quite different (asymmetrical) at any given time. Segments B, C, and D are essentially symmetrical cases where thicknesses on conjugate flanks differ by only 100–200 m (Figure 8). Segment I is a prominent example of an asymmetrical case (Figure 8h). Crust on the west flank of this segment is 0.3–1.5 km thicker than that on the east flank, and this asymmetry has been maintained for at least the past 10 Myr.

The degree and direction of symmetry/asymmetry of crustal thickness can vary with time. In segment G, for example, crustal thickness is up to 1 km thinner on the west flank prior to ~13 Ma (Figure 8g), when this crust was bounded by two inside corners. Since ~5 Ma, the west flank of this segment has been about 0.5 km thicker.

5.4. Correlations Between Crustal Thickness and Seafloor Morphology

Variations in crustal thickness are closely correlated with patterns of seafloor morphology. Thick-crust areas usually exhibit linear to curvilinear ridge-parallel topography in the form of relatively isostatically compensated abyssal hills. The abyssal hills are created by normal faults with limited throw and generally extend over the full lengths of segments (Figure 11); side-scan sonar images commonly show volcanic cones on tops of the fault blocks (Figures 11c and 11d, insets). In contrast, thin-crust areas (Figure 12, right side) are associated with large nonisostatic topography (Figure 12h), suggesting large degrees of stress-supported topography. The topography in these areas is typically blocky to irregular, faults have large throws, and volcanic features are rarely observed.

Figures 11 and 12 illustrate how these correlations are expressed in crustal conjugates. Figure 11 shows a case of symmetrical conjugates along the center of segment E between anomalies ~3An and ~5n; the conjugates are relatively symmetrical in terms of having thick crust, similar seafloor depth, long linear faults, and volcanic features. Near the segment ends, the morphologic patterns of conjugates become antisymmetric, with thinner IC crust showing higher-amplitude, more irregular topography. Figure 12 shows a case of significantly asymmetrical crustal thickness between conjugate ridge flanks over the full length of segment I between the ridge axis and anomaly ~3n. The west flank, which has thick crust, is dominated by ridge-parallel, low-amplitude abyssal hills that are relatively linear and isostatically compensated. In the thin crust of the conjugate east flank, the topography is irregular, high amplitude, and largely stress supported. Numerous seamounts appear on the west flank but they are rare on the east flank. Dante's Domes megamullion is located at the southern end of the east flank crust (Figure 12) in seafloor younger than anomaly ~2n. The megamullion consists of a set of broad domes with surface corrugations elongated in the flow line direction. It was formed by long-lived (~1.3 Myr) detachment faulting that appears to have exhumed lower crust and possibly upper mantle [*Tucholke et al*., 2001]. It stands out as a nonisostatic topographic high in an area of thin crust and it exhibits morphology very different from its west flank conjugate.

Figure 11 Example of ridge-flank conjugates (~11 Ma to 6 Ma) that show similar morphology and crustal thickness. (a and b) East and west flank bathymetry (100 m contour interval), (c and d) side-scan sonar imagery, (e and f) crustal thickness variations (0.1 km contour interval), and (g and h) nonisostatic topography (100 m contour interval). ICs and OCs are labeled near segment boundaries (dotted lines). Larger-scale inserts in Figures 11c and 11d show volcanic cones (circular features) along the tops of fault blocks. In Figure 11c, the insonification direction is to the NNW, and in Figure 11d, it is to the NE; thus, faults that dip toward the ridge axis are emphasized on both ridge flanks. Most normal faults (away from ICs) have limited throw, and they form regular patterns of long, linear abyssal hills. Faults in the thinner crust at ICs have larger throws and are more irregular. Note the general symmetry of structures at the segment center of the conjugates and the strong antisymmetry in the IC/OC conjugates.

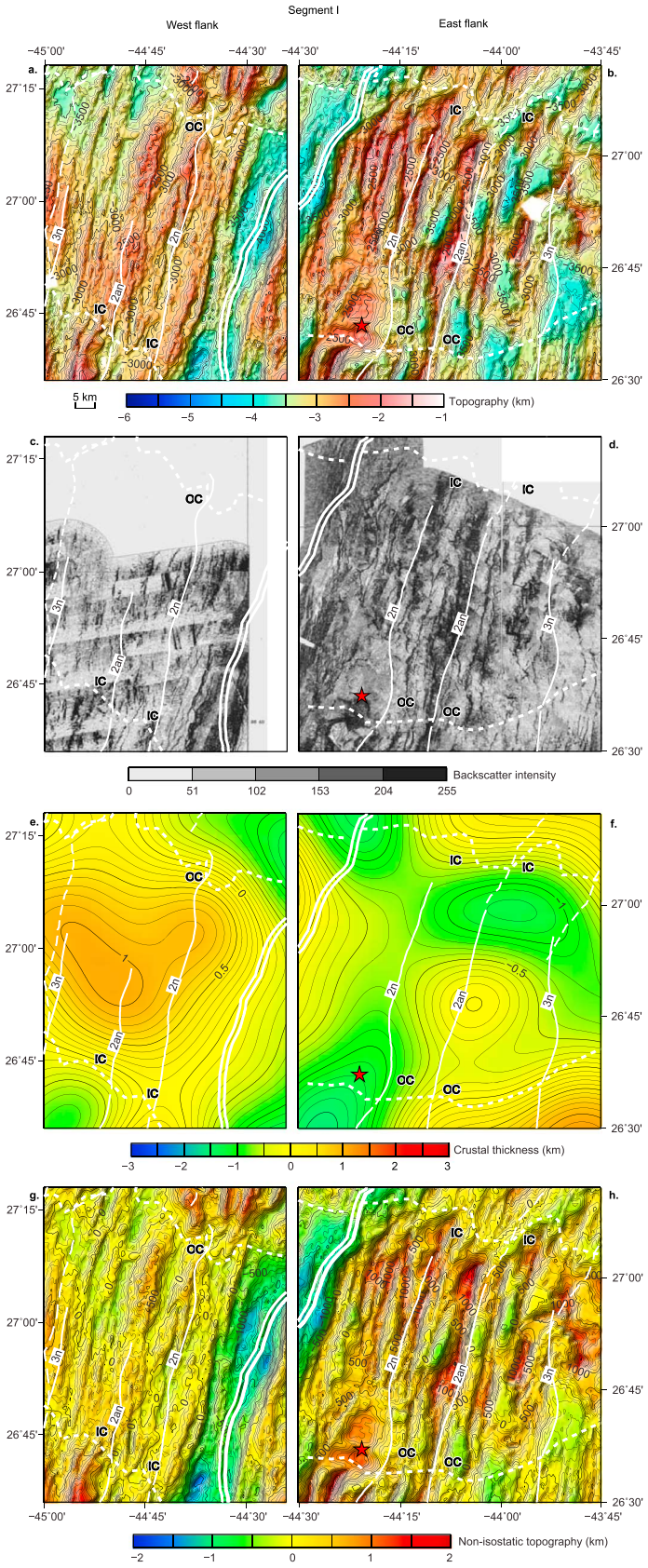

Figure 12

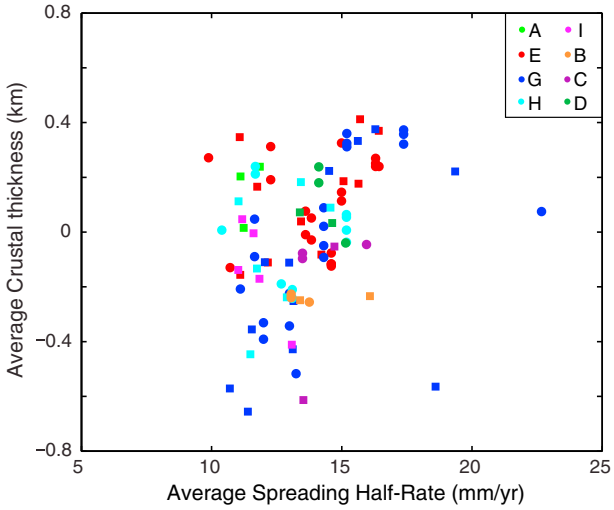

Figure 13. Plot of average crustal thickness versus average spreading half rate. Crustal thickness is the average of both ridge flanks of a spreading segment at a given time (Figure 9a), and spreading half rate is the average rate of the two flanks of the segment at that time. Squares locate data at major isochrons, which fall at boundaries between intervals of calculated spreading rate; at these locations, spreading rates are taken as averages of the rates in the two adjacent time intervals. There is no apparent correlation between crustal thickness and spreading rate.

5.5. Intersegment Variations

There are no consistent correlations in across-axis crustal thickness patterns from one segment to another through time (Figure 9a). Although crustal production at some times was similar between adjacent segments (e.g., segments E and G at ~18–10 Ma), for the most part the amount of melt introduced into any given segment has been independent from that introduced in adjacent segments. Segments H and I, and E and G, for example, exhibit opposite variations in crustal thickness at about 10 to 5 Ma. Thus, the short-term, 2–3 Myr variations in crustal thickness appear to be controlled at the scale of individual spreading segments.

6. Regional Variations

Regionally, the thickest average crust is present at ~19–12 Ma (Figure 9b), due primarily to thicker crust on the eastern ridge flank. The thinnest crust appears at ages older than ~22 Ma and younger than ~5 Ma. For the former, thin crust is present on both flanks in a roughly symmetrical pattern (Figure 3b). In crust younger than 5 Ma, the east flank exhibits thin crust while the west flank has mostly normal and even locally thickened crust, resulting in a strongly asymmetric pattern (Figures 3b and 9b). A comparison of average crustal thickness versus average spreading rate within individual segments (Figure 13) shows large scatter and no correlation between the two variables. The same lack of correlation holds true in a comparison of average crustal thickness versus average spreading rate on each flank within individual segments, and for spreading rate asymmetry and crustal thickness asymmetry in individual spreading segments.

7. Discussion

7.1. Along- and Across-Isochron Changes in Model Crustal Thickness

It has long been recognized that 3-D mantle upwelling at slow-spreading ridges can lead to large along-axis variations in crustal thickness, caused by enhanced melt input at segment centers and reduced melt supply near segment ends [e.g., *Lin et al.*, 1990; *Lin and Phipps Morgan*, 1992]. The pattern of thick crust at segment centers and thinner crust toward segment ends holds reasonably well throughout our study area (Figure 3b). However, thinner crust near segment ends does not have equal thicknesses on opposing sides of the spreading axis. The thinnest crust has formed primarily at ICs while crust at conjugate OCs typically is thicker (e.g., Figures 3b and 7). This IC/OC asymmetry has been well documented and is attributed to enhanced, longer-lived normal faulting at inside corners [e.g., *Dick et al.*, 1981, 1991; *Brown and Karson*, 1988; *Karson*, 1990; *Tucholke and Lin*, 1994; *Tucholke et al.*, 1997].

Temporal, across-isochron changes in model crustal thickness are observed at two different scales: a short timescale of 2–3 Myr, and a longer timescale of $>$10 Myr. The shorter-term variations of a few million years are observed in other areas of the MAR [*Rommevaux et al.*, 1994; *Gente et al.*, 1995; *Pariso et al.*, 1995;

Figure 12 Example of ridge-flank conjugates (~5 Ma to present) that show strongly differing crustal thickness and morphology. Panels are as described in Figure 11. The ridge axis is shown by a white double line. The star on the east flank panels locates Dante's Domes megamullion, formed by long-lived detachment faulting [*Tucholke et al.*, 2001]. East flank crust is much thinner than west flank crust, and it is dissected by larger-offset, more irregular faults. These differences overwhelm differences between conjugate ICs and OCs.

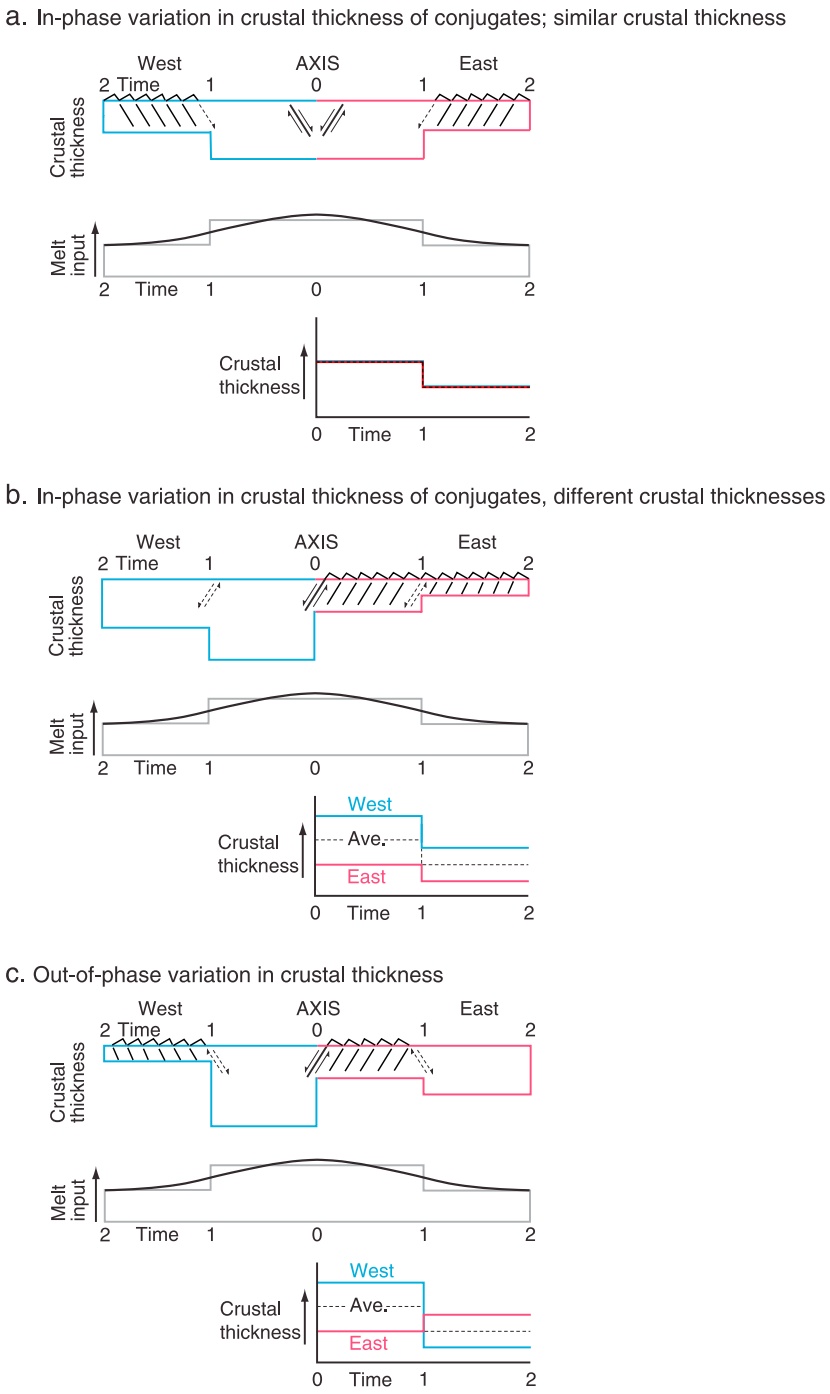

Figure 14. Schematic models showing how interactions between normal-fault patterns and variable melt supply at the MAR axis can explain observed variations in crustal thickness and seafloor morphology. In all instances, melt input is shown as increasing by one unit with time; this is shown as a step function, but it likely varies more gradually (smooth curve). (a) Intensity/duration of normal faulting is equally distributed between opposing rift-valley walls through time; thus, crustal thicknesses and seafloor morphology are the same in conjugate ridge-flank parcels. There is less melt input at time 2 to 1, so enhanced tectonic extension creates higher-amplitude topography on both ridge flanks. (b) Larger-offset normal faults consistently concentrate in the east wall of the rift valley through time (former faults indicated by dashed arrows), and melt is partitioned more to the west flank. This results in different crustal thicknesses in conjugate ridge-flank parcels even though thickness changes are in-phase. Thinner crust on the east flank is more strongly faulted and has higher-amplitude topography than thicker crust on the west flank. (c) Larger-offset normal faults alternate from one wall of the axial valley to the other wall through time. This causes crustal-thickness changes to be out of phase between conjugate ridge-flank parcels; larger-offset normal faults create more irregular topography on the ridge flank with thinner crust.

Bonatti et al., 2003] and they appear to be a general phenomenon of crustal accretion on this slow-spreading ridge. Because the variations on conjugate ridge flanks are commonly in-phase (Figure 8), they most likely are related to processes taking place at the ridge axis.

7.2. Origin of Temporal Changes in Model Crustal Thickness

7.2.1. Serpentinization

Serpentinization can reduce mantle density to values similar to that of oceanic crust; thus, not accounting for this possible density change can influence our model results. We expect that if mantle serpentinization occurs, it would be mainly in zones of thinner crust where deep faults can conduct fluids into the mantle, i.e., in NTDs and during intervals of reduced melt input. Not accounting for potential serpentinization in zones of thin crust would result in our crustal thickness model underpredicting the magnitude of thickness variations (Figure 4), i.e., serpentinites in thin-crust zones dampen apparent crustal thickness changes. Thus, serpentinization cannot explain the observed temporal changes in model crustal thickness.

7.2.2. Changes in Melt Input

The most likely explanation for the short-term temporal variations in model crustal thickness is cyclic changes in melt input at the ridge axis. One possible way to accomplish this is by intermittent release of melt from a subaxial magma reservoir. In this mechanism, magma rises as a result of gravitational instability under spreading centers [*Scott and Stevenson*, 1984; *Whitehead et al*., 1984; *Schouten et al*., 1985], accumulates in a magma reservoir, and is episodically expelled to form ocean crust. However, it seems unlikely that such a large magma reservoir could be contained beneath the ridge axis for several million years at a time, or that its release would be as gradual as suggested by the character of the observed crustal thickness changes. Furthermore, if large magma chambers were present beneath the Mid-Atlantic Ridge, they should be easy to detect seismically, but seismic experiments indicate that they are either absent [e.g., *Detrick et al*., 1990; *Hooft et al*., 2000; *Zhao et al*., 2012] or are small relative to the length of spreading segments [*Singh et al*., 2006]. Therefore, we discount intermittent release of melt from a subaxial magma reservoir as a reasonable mechanism.

Another possibility is that production of melt is related to temperature variations in the mantle. Temperature oscillations on a timescale of ~3–6 Myr have been surmised for the Iceland plume [*Parkin et al*., 2007; *Parkin and White*, 2008]. Considering the local spreading rate, this corresponds to spatial scale of 30 km up to a few hundred kilometers. This is at and well above the high end of spatial scales observed in our study, so temperature oscillations on a timescale of several million years do not seem to be a likely explanation for the observed variations in melt production.

A third possibility is that compositional changes in the mantle induced by melt extraction beneath the ridge axis create imbalances in mantle buoyancy that can drive intermittent convective rolls and increased melting. *Bonatti et al*. [2003] invoked this mechanism to explain 3–4 Myr cyclicity in crustal thickness and degree of mantle melting over an across-isochron transection at the Vema Fracture Zone in the central Atlantic. They inferred from geochemical data that the mantle had uniform composition, and thus, melting of heterogeneous mantle could not be responsible for the observed patterns.

Melting of heterogeneous mantle, however, remains a possible explanation for the short-term variation in melt production in our study area. The observed across-isochron changes between thick and thin crust are at spatial scales of ~25–50 km, which would imply heterogeneities of similar scale in the mantle. It is well established that lateral changes in mantle composition and water content occur on the MAR over distances less than ~100 km [e.g., *Bonatti et al*., 1992], so this is a reasonable expectation. As shown in Figure 9a, short-term temporal variations in crustal thickness for the most part do not correlate from one segment to another, so melt supply in each segment appears to be independent of that in adjacent segments. Ultimately, a sampling/geochemical study will be needed to resolve the question of whether a dynamic mechanism or mantle heterogeneity best explains the short-period temporal changes in melt supply.

Like *Bonatti et al*. [2003], we also see long-term trends in melt production, with increasing production from about 25 Ma to 17 Ma and declining production since ~13 Ma (Figure 9b). This timescale is similar to the long-term variation (~15–20 Myr) observed at the Vema Fracture Zone [*Bonatti et al*., 2003]. At this scale, changes in melt supply could be due to either mantle heterogeneity or variations in mantle temperature. We observe no correlation between average model crustal thickness and average spreading rate (Figure 13), so we conclude that melt input into the crust is unrelated to the rate of plate separation.

7.2.3. Magmatism and Tectonism

The degree and character of tectonism at the MAR axis are controlled by levels of magmatism. At constant or slowly changing spreading rates, a deficiency in melt input would result in thinner crust; the melt deficiency would also require increased tectonic extension to accommodate the full rate of plate separation, and this further thins the crust. During intervals when thicker crust is accreted, we observe that normal faults tend to be long and linear, have limited throw, and thus produce regular patterns of relatively low-relief abyssal hills (Figure 11). In contrast, irregular topography and large-throw faults are limited to zones of thinner crust (Figure 12).

Further aspects of this pattern involve symmetry and asymmetry of tectonic features in conjugate crustal parcels on opposing sides of the spreading axis. In places where thicker crust is accreted, low-relief abyssal hills are produced symmetrically on both sides of the rift axis (see segment center, Figure 11) [*Shaw and Lin*, 1996; *Buck et al*., 2005]. However, the irregular, high-relief topography created in zones of low melt supply usually is asymmetrically distributed to one side of the rift axis (Figure 12). Such asymmetry is similar to that observed between ICs and OCs [*Tucholke and Lin*, 1994], which has been attributed to enhanced normal faulting and the presence of detachment faults (here considered to be normal faults with very long-lived slip, e.g., $>$~1 Myr) at ICs. Lower crust and upper mantle can be exhumed in IC footwalls, while the OC hanging wall consists primarily of accreted magma, resulting in differences both in lithospheric structure and crustal composition on the two sides of the rift axis [*Tucholke and Lin*, 1994; *Tucholke et al*., 1996a, 1998, 2008; *Cann et al*., 1997; *Okino et al*., 2004; *Smith et al*., 2006; *Olive et al*., 2010].

This kind of asymmetry between IC/OC conjugates at segment ends appears throughout the study area (e.g., Figures 11, S2, S7, and S8). However, the asymmetry often is not confined to segment ends but instead is observed over the entire length of a segment (e.g., Figures 12, S3–S6, S9, and S10). *Escartin et al.* [2008] examined the MAR axis from 12.5°N to 30°N and suggested that up to ~50% of this length may be affected by asymmetric "detachment" faulting, including the full lengths of segments E through I in our study area. Although we identify a detachment fault only at Dante's Domes megamullion in segment I (Figure 12), it is clear that all these segments are asymmetric at the ridge axis due to longer-lived normal faults that have created higher-amplitude, irregular topography on the east flank (Figures 12 and S4–S6). This asymmetry is consistent with our observations of thinner crust on the east side of the MAR axis in all these segments over the past 3–5 Myr (Figures 3b and 8). Moreover, the asymmetry is associated with significant differences in the calculated spreading rate on the two flanks of the ridge during this period. The more tectonized east flank has spread 2 to 5 mm yr^{-1} faster than its west flank conjugate (Figure 6); thus, during this period of reduced melt supply, tectonic extension has outpaced crustal accretion and the spreading axis has migrated relatively westward.

The factors that cause tectonic extension to concentrate on one wall of the rift valley are a subject of debate. In the instance of IC/OC differences, a case can be made that enhanced normal faulting at ICs relates to the fact the ICs are adjacent to two "free" plate boundaries (i.e., the spreading axis and the transform fault or NTD) [e.g., *Kuo et al*., 1984; *Chen and Lin*, 1999]. This allows preferential tectonic uplift of ICs compared to OCs, which are locked to older crust across the inactive discontinuity. This idea can be extended to explain why an entire segment is asymmetrical in the instance where it is bounded by oppositely directed offsets at its ends (e.g., Figure S9), but it does not account for segments that are completely asymmetrical when the bounding NTDs have the same offset directions (e.g., segments E, G, and H; Figures 2 and 3). One possible explanation for the latter case is that the preferred locations of magma emplacement versus tectonic extension on the sides of the rift valley are influenced by relative motion of the plate boundary over the upwelling mantle. If this were true, however, we would expect to see the direction of asymmetry to be relatively constant all along the plate boundary, and this is not the case.

Another possibility is that preferred locations of tectonic extension reflect asymmetric distribution of heat and melt in chemically heterogeneous mantle upwelling beneath the plate boundary. Although melt may be ultimately focused toward the ridge axis at shallow levels, advection of heat in the mantle and heat introduced by fractional crystallization might preferentially occur beneath one ridge flank and thus thin the lithosphere on that flank, which in turn could lead to asymmetry in the degree of tectonic extension. This idea is consistent with the concept, discussed above, that the mantle is heterogeneous on scales of tens of kilometers (roughly the "segment scale") to $>$100 km. It also takes into account the unlikelihood that heterogeneities in upwelling mantle will be perfectly centered beneath the spreading ridge axis. Finally, it is possible that the asymmetry is simply random. Discriminating among these possibilities will be very difficult,

but it might be best approached by seismic and electromagnetic studies that test for asymmetries in mantle properties beneath the rift axis.

7.3. Model of Crustal Accretion

As discussed above, the level of melt input at the MAR axis controls both crustal thickness and the degree of tectonic extension recorded in the ridge flanks. Because the melt is supplied at the spreading axis, we might expect to see approximate symmetry in crustal thickness and tectonic patterns between conjugate ridge flanks, but this is not always the case. Although crustal-thickness changes on the conjugates are commonly in phase (Figure 8), actual thicknesses at any point in time are often significantly different, and in some cases the thickness changes are directly out of phase (Figure 8g). Considering the phase relations and comparing actual crustal thicknesses in ridge-flank conjugates, we recognize three patterns of crustal accretion, as described below.

In the first pattern (Figure 14a), crustal thickness variations are in-phase between conjugate ridge flanks, and melt is partitioned equally to the two sides of the rift axis so that thicknesses are symmetrical (e.g., Figure 8, segments B, C, and D). Inward facing normal faults are symmetrically distributed on the two sides of the rift axis, and they retain this configuration as melt input waxes and wanes through time. This pattern usually is observed in thicker crust (Figure 14a, at time 1 to 0), where long, linear normal faults with limited throws develop. An example is in segment E at ~18–14 Ma where the crust is relatively thick and regular abyssal hills are present (Figures 8e and S7). Thinner crust can have similar symmetry but the normal faults on the two ridge flanks have large throws and the topography is more irregular (Figure 14a, at time 2 to 1). Crust in segment G at ~7–5 Ma (Figure 8f) shows these characteristics (Figure S8).

The second pattern is characterized by in-phase crustal-thickness variations but asymmetrical crustal thicknesses on conjugate ridge flanks (Figure 14b). In this case longer-lived faults are concentrated on one side of the rift valley and this asymmetry is maintained through successive magmatic cycles. The tendency of tectonic extension to be partitioned to one side of the axis and melt accretion to the other side results in both crustal thickness and morphological differences between ridge flanks, even though the magmatic phase is the same. A prominent example is in segment I where west flank crust has consistently been much thicker than the conjugate east flank (Figure 8h). The much thinner crust on the east flank shows larger-offset faults (including the detachment fault at Dante's Domes) and more rugged topography than the west flank (Figure 12). This is also the kind of asymmetry that is commonly observed in IC/OC pairs near segment ends, sometimes extending well into segment centers (e.g., segment E at ~6–3 Ma; Figures 8e and S2). The pattern develops readily where a segment has ICs at both ends on one side of the spreading axis (e.g., segment G at ~13–19 Ma, Figures 8f and S9), but it also occurs where ICs and OCs alternate along a segment.

Crustal conjugates in the third pattern have out-of-phase crustal-thickness variations, as well as (necessarily) asymmetrical crustal thicknesses except at phase crossovers (Figure 14c). We explain this pattern by one wall of the rift valley again being dominated by longer-lived normal faults, but with that faulting alternating between opposing valley walls over time; melt input at the rift axis may or may not be varying at the same time. At time 2 to 1 in Figure 14c, enhanced tectonic extension in the west wall of the rift valley resulted in thinner, more irregular crust on the west flank, while a shift of the longer-lived faults to the east wall at time 1 to 0 reversed this pattern. A good example of this is in segment H (Figure 8g). At ~8–3 Ma, longer-lived normal faults were concentrated in the west wall of the rift valley, and the west flank crust is thinner and shows more irregular, higher-amplitude topography than the conjugate east flank (Figure S10). This pattern was reversed after ~3 Ma, with major faulting shifting to the east rift-valley wall, and thinner, more tectonized and irregular crust appearing on the east ridge flank (Figure S6).

8. Conclusions

We conducted a detailed study of crustal accretion on the Mid-Atlantic Ridge from 25°N to 27°30′N, and from the ridge axis out to ~27 Ma crust, by analyzing high-resolution multibeam bathymetry, shipboard gravity, long-range side-scan sonar images, and magnetic anomaly data on the conjugate ridge flanks. Our main conclusions are summarized below.

Model crustal thickness derived from gravity modeling generally varies up to ±2 km from a reference thickness of 6 km. Considering effects of sediment thickness and possible serpentinization that were not

modeled, these are probably minimum variations in true crustal thickness. There are substantial variations along isochrons within spreading segments. Segment centers usually have the thickest crust, outside corners at segment ends have intermediate-thickness crust, and inside corners exhibit the thinnest crust.

Across-isochron variations in crustal thickness occur on two timescales. On the longer timescale ($>$ ~10 Myr), crust was relatively thin prior to 22 Ma, it thickened to maximum values between ~19 Ma and 12 Ma, and it has thinned since that time. The long-term changes in magma production represented by this variation may be due to long-wavelength thermal or compositional changes in the mantle. Average crustal thickness has been independent of spreading rate through time.

Superimposed on the long-term variation, episodic crustal thickening and thinning have occurred every ~2–3 Myr. These shorter-term variations are generally in-phase between conjugate ridge flanks. We attribute them to cyclic changes in melt production, which may be controlled by (1) differential melting of mantle that is chemically heterogeneous on length scales of ~25–50 km or (2) dynamic instability and convection in the upper mantle driven by buoyancy changes associated with melt extraction. There are no consistent correlations of these cyclic changes from one segment to another, indicating that melt production is controlled independently in each segment.

Although cycles of increased and decreased model crustal thickness are mostly in-phase between opposing ridge flanks of a spreading segment, actual crustal thickness values at any one time within a cycle can be quite asymmetrical between the conjugates. We attribute this asymmetry to the predominance of longer-lived faults on one side or the other of the rift axis, with thinner crust consistently being produced on the more tectonized side of the axis. Spreading rates on the ridge flank with more highly faulted, thinner crust commonly are higher than on the conjugate flank, most notably over the past 3–5 Myr in four segments in the central part of our survey area.

Morphologic features on the seafloor are highly correlated with variations in crustal thickness. Thicker crust is associated with long, linear normal faults that have limited throw, resulting in regularly spaced abyssal hills that often are capped by small volcanic cones. Thin crust exhibits larger-offset normal faults and is characterized by elevated, high-amplitude, and often irregular topography that shows few volcanic features. Thus, crustal morphology by itself is a useful proxy for predicting crustal thickness and potential seafloor exposure of lower-crustal and upper mantle rocks.

Acknowledgments

We are grateful to the crew and science parties of the ARSRP, MAREAST, MODE94, and MODE98 expeditions for their contributions to data acquisition. We thank Allegra Hosford for help in deriving spreading rate information from the magnetic anomalies, and we thank Roger Searle and an anonymous reviewer for detailed reviews that helped us to improve the manuscript. Figures were drawn using the GMT software of *Wessel and Smith* [1998]. This study was funded by Chinese Natural Science Foundation grant 41206034 and Chinese Postdoc Scholarship award 2012M511130 (T.W.), by Ministry of Science and Technology 973 Project award 2012CB417303, and by the WHOI Henry Bryant Bigelow Chair (J.L.). ARSRP and MAREAST data acquisition was funded by Office of Naval Research grant N00014-90-J-6121 and by U.S. National Science Foundation grant OCE-9503561, respectively. For data accessing, please contact jlin@whoi.edu.

References

Allerton, S., J. Escartin, and R. C. Searle (2000), Extremely asymmetric magmatic accretion of oceanic crust at the ends of slow-spreading ridge segments, *Geology*, *28*, 179–182.

Bonatti, E., A. Peyve, P. Kepezhinskas, N. Kurentsova, M. Seyler, S. Skolotnev, and G. Udintsev (1992), Upper mantle heterogeneity below the Mid-Atlantic Ridge, 0°–15°N, *J. Geophys. Res.*, *97*, 4461–4476, doi:10.1029/91JB02838.

Bonatti, E., M. Ligi, D. Brunelli, A. Cipriani, P. Fabretti, V. Ferrante, L. Gasperini, and L. Ottolini (2003), Mantle thermal pulses below the Mid-Atlantic Ridge and temporal variations in the formation of oceanic lithosphere, *Nature*, *423*, 499–505.

Brown, J. R., and J. A. Karson (1988), Variations in axial processes on the Mid-Atlantic Ridge: The median valley of the MARK area, *Mar. Geophys. Res.*, *10*, 109–138.

Buck, W. R., L. L. Lavier, and A. N. B. Poliakov (2005), Modes of faulting at mid-ocean ridges, *Nature*, *434*, 719–723.

Cann, J. R., D. K. Blackman, D. K. Smith, E. McAllister, B. Janssen, S. Mello, E. Avgerinos, A. R. Pascoe, and J. Escartin (1997), Corrugated slip surfaces formed at ridge-transform intersections on the Mid-Atlantic Ridge, *Nature*, *385*, 329–332.

Cannat, M. (1993), Emplacement of mantle rocks in the seafloor at mid-ocean ridges, *J. Geophys. Res.*, *98*, 4163–4172, doi:10.1029/92JB02221.

Cannat, M., et al. (1995), Thin crust, ultramafic exposures, and rugged faulting patterns at the Mid-Atlantic Ridge (22°-24°N), *Geology*, *23*, 49–52.

Cannat, M., D. Sauter, V. Mendel, E. Ruellan, K. Okino, J. Escartin, V. Combier, and M. Baala (2006), Modes of seafloor generation at a melt-poor ultraslow-spreading ridge, *Geology*, *34*, 605–608.

Chen, J. Y., and J. Lin (1999), Mechanisms for the formation of ridge-axis topography at slow spreading ridges: A lithospheric plate flexure model, *Geophys. J. Int.*, *136*, 8–18.

Detrick, R. S., J. C. Mutter, P. Buhl, and I. I. Kim (1990), No evidence from multichannel reflection data for a crustal magma chamber in the MARK area on the Mid-Atlantic Ridge, *Nature*, *347*, 61–64.

Dick, H. J. B., G. Thompson, and W. B. Bryan (1981), Low angle faulting and steady-state emplacement of plutonic rocks at ridge-transform intersections (abstract), *Eos Trans. AGU*, *62*, 406.

Dick, H. J. B., H. Schouten, P. S. Meyer, D. G. Gallo, H. Bergh, R. Tyce, P. Patriat, K. T. M. Johnson, J. Snow, and A. Fischer (1991), Tectonic evolution of the Atlantis II Fracture Zone, in *Proceedings of the Ocean Drilling Program, Scientific Results*, vol. 118, edited by R. P. Von Herzen and P. T. Robinson, pp. 359–398, Ocean Drill. Program, College Station, Tex.

Escartin, J., and J. Lin (1995), Ridge offsets, normal faulting, and gravity anomalies of slow-spreading ridges, *J. Geophys. Res.*, *100*, 6163–6177, doi:10.1029/94JB03267.

Escartin, J., and J. Lin (1998), Tectonic modification of axial crustal structure: Evidence from spectral analyses of residual gravity and bathymetry of the Mid-Atlantic Ridge flanks, *Earth Planet. Sci. Lett.*, *154*, 279–293.

Escartin, J., G. Hirth, and B. Evans (2001), Strength of slightly serpentinized peridotites: Implications for the tectonics of oceanic lithosphere, *Geology*, *29*, 1023–1026.

Escartin, J., D. K. Smith, J. Cann, H. Schouten, C. H. Langmuir, and S. Escrig (2008), Central role of detachment faults in accretion of slow-spreading oceanic lithosphere, *Nature*, *455*, 790–795.
Fujimoto, H., N. Seama, J. Lin, T. Matsumoto, T. Tanaka, and K. Fujioka (1996), Gravity anomalies of the Mid-Atlantic Ridge north of the Kane fracture zone, *Geophys. Res. Lett.*, *23*, 3431–3434, doi:10.1029/96GL02080.
Fujioka, K., H. Chiba, T. Naganuma, H. Masuda, T. Oomori, P. A. Rona, B. E. Tucholke, T. Ishihara, and H. Yamamoto (1999), Hydrothermal activity and architecture of slow-spreading ridge at TAG and Rainbow hydrothermal fields and Dante's Domes megamullion in the Mid-Atlantic Ridge – MODE '98 Leg 2 MEGATRAIN cruise results summary, *JAMSTEC J. Deep Sea Res. 2. Geol. Geochem. Geophys. Dive Surv.*, *15*, 39–49.
Fujiwara, T., J. Lin, T. Matsumoto, P. B. Kelemen, B. E. Tucholke, and J. F. Casey (2003), Crustal evolution of the Mid-Atlantic Ridge near the Fifteen-Twenty Fracture Zone in the last 5 Ma, *Geochem. Geophys. Geosyst.*, *4*(3), 1024, doi:10.1029/2002GC000364.
Gente, P., R. A. Pockalny, C. Durand, C. Deplus, M. Maia, G. Ceuleneer, C. Mevel, M. Cannat, and C. Laverne (1995), Characteristics and evolution of the segmentation of the Mid-Atlantic Ridge between 20°N and 24°N during the last 10 million years, *Earth Planet. Sci. Lett.*, *129*, 55–71.
Gracia, E., D. Bideau, R. Hekinian, Y. Lagabrielle, and L. M. Parson (1997), Along-axis magmatic oscillations and exposure of ultramafic rocks in a second-order segment of the Mid-Atlantic Ridge (33°43′N to 34°07′N), *Geology*, *25*, 1059–1062.
Hooft, E. E. E., R. S. Detrick, D. R. Toomey, J. A. Collins, and J. Lin (2000), Crustal thickness and structure along three contrasting spreading segments of the Mid-Atlantic Ridge, 33.5°-35°N, *J. Geophys. Res.*, *105*, 8205-8226. doi:10.1029/1999JB900442.
Jaroslow, G. E. (1996), The geological record of oceanic crustal accretion and tectonism at slow-spreading ridges, PhD thesis, 210 pp., MIT/WHOI Joint Program in Oceanography, Woods Hole, Mass.
Karson, J. A. (1990), Seafloor spreading on the Mid-Atlantic Ridge: Implications for the structure of ophiolites and oceanic lithosphere produced in slow-spreading environments, in *Proceedings of the Symposium TROODOS 1987*, edited by J. Malpas et al., pp. 547–555, Geol. Surv. Dept., Nicosia, Cyprus.
Klitgord, K. D., and H. Schouten (1986), Plate kinematics of the central Atlantic, in *The Geology of North America, Vol. M, The Western North Atlantic Region*, edited by P. R. Vogt and B. E. Tucholke, pp. 351–358, Geol. Soc. of Am., Boulder, Colo.
Kuo, B. Y., and D. W. Forsyth (1988), Gravity anomalies of the ridge-transform system in the South Atlantic between 31° and 34.5°S: Upwelling centers and variations in crustal thickness, *Mar. Geophys. Res.*, *10*, 205–232.
Kuo, B. Y., W. J. Morgan, and D. W. Forsyth (1984), Asymmetry in topography of the crestal mountains near a ridge–transform intersection, *Eos Trans. AGU*, *65*, 274.
Lin, J., and J. Phipps Morgan (1992), The spreading rate dependence of three-dimensional mid-ocean ridge gravity structure, *Geophys. Res. Lett.*, *19*, 13–16, doi:10.1029/91GL03041.
Lin, J., G. M. Purdy, H. Schouten, J. C. Sempere, and C. Zervas (1990), Evidence from gravity data for focused magmatic accretion along the Mid-Atlantic Ridge, *Nature*, *344*, 627–632.
MacLeod, C. J., et al. (2002), Direct geological evidence for oceanic detachment faulting: The Mid-Atlantic Ridge, 15°45′N, *Geology*, *30*, 879–882.
Maia, M., and P. Gente (1998), Three-dimensional gravity and bathymetry analysis of the Mid-Atlantic Ridge between 20°N and 24°N: Flow geometry and temporal evolution of the segmentation, *J. Geophys. Res.*, *103*, 951–974, doi:10.1029/97JB01635.
Ogg, J. G. (2012), Geomagnetic polarity time scale, in *The Geologic Time Scale 2012*, edited by F. M. Gradstein et al., pp. 85–113, Elsevier B.V., Amsterdam, doi: 10.1016/B978-0-444-59425-9.00005-6.
Okino, K., K. Matsuda, D. M. Christie, Y. Nogi, and K. Koizumi (2004), Development of oceanic detachment and asymmetric spreading at the Australian-Antarctic Discordance, *Geochem. Geophys. Geosyst.*, *5*, Q12012, doi:10.1029/2004GC000793.
Olive, J.-A., M. D. Behn, and B. E. Tucholke (2010), The structure of oceanic core complexes controlled by the depth distribution of magma emplacement, *Nat. Geosci.*, *3*, 491–495, doi:10.1038/NGEO888.
Pariso, J. E., J. C. Sempere, and C. Rommevaux (1995), Temporal and spatial variations in crustal accretion along the Mid-Atlantic Ridge (29°-31°30′N) over the last 10 m.y.: Implications from a three-dimensional gravity study, *J. Geophys. Res.*, *100*, 17,781–17,794, doi:10.1029/95JB01146.
Parker, R. L. (1972), The rapid calculation of potential anomalies, *Geophys. J. R. Astron. Soc.*, *31*, 447–455.
Parkin, C. J., and R. S. White (2008), Influence of the Iceland mantle plume on oceanic crust generation in the North Atlantic, *Geophys. J. Int.*, *173*, 168–188.
Parkin, C. J., Z. C. Lunnon, R. S. White, and P. A. F. Christie (2007), Imaging the pulsing Iceland mantle plume through the Eocene, *Geology*, *35*, 93–96.
Rognstad, M. (1992), HAWAII MR1: A new underwater mapping tool International Conference on Signal Processing and Technology, pp. 900–905.
Rommevaux, C., C. Deplus, P. Patriat, and J. C. Sempere (1994), Three-dimensional gravity study of the Mid-Atlantic Ridge: Evolution of the segmentation between 28°N and 29°N during the last 10 m.y., *J. Geophys. Res.*, *99*, 3015–3029, doi:10.1029/93JB02361.
Schouten, H., K. D. Klitgord, and J. A. Whitehead (1985), Segmentation of mid-ocean ridges, *Nature*, *317*, 225–229.
Scott, D. R., and D. J. Stevenson (1984), Magma solitons, *Geophys. Res. Lett.*, *11*, 1161–1164, doi:10.1029/GL011i011p01161.
Searle, R. C., P. A. Cowie, N. C. Mitchell, S. Allerton, C. J. MacLeod, J. Escartin, S. M. Russell, P. A. Slootweg, and T. Tanaka (1998), Fault structure and detailed evolution of a slow spreading ridge segment: The Mid-Atlantic Ridge at 29°N, *Earth Planet. Sci. Lett.*, *154*, 167–183.
Sempere, J. C., P. Blondel, A. Briais, T. Fujiwara, L. Geli, N. Isezaki, J. E. Pariso, L. Parson, P. Patriat, and C. Rommevaux (1995), The Mid-Atlantic Ridge between 29°N and 31°30′N in the last 10 Ma, *Earth Planet. Sci. Lett.*, *130*, 45–55.
Sempere, J.-C., J. Lin, H. S. Brown, H. Schouten, and G. M. Purdy (1993), Segmentation and morphotectonic variations along a slow-spreading center: The Mid-Atlantic Ridge 24°-30°40′N, *Mar. Geophys. Res.*, *15*, 153–200.
Shaw, P. R. (1992), Ridge segmentation, faulting and crustal thickness in the Atlantic Ocean, *Nature*, *358*, 490–493.
Shaw, P. R., and J. Lin (1993), Causes and consequences of variations in faulting style at the Mid-Atlantic Ridge, *J. Geophys. Res.*, *98*, 21,839–21,851, doi:10.1029/93JB01565.
Shaw, W. J., and J. Lin (1996), Models of ocean ridge lithospheric deformation: Dependence on crustal thickness, spreading rate, and segmentation, *J. Geophys. Res.*, *101*, 17,977–17,993, doi:10.1029/96JB00949.
Singh, S. C., W. C. Crawford, H. Carton, T. Seher, V. Combier, M. Cannat, J. P. Canales, D. Dusunur, J. Escartin, and J. M. Miranda (2006), Discovery of a magma chamber and faults beneath a Mid-Atlantic Ridge hydrothermal field, *Nature*, *442*, 1029–1032, doi:10.1038/nature05105.
Sloan, H., and P. Patriat (1992), Kinematics of the North American-African plate boundary between 28° and 29°N during the last 10 Ma: Evolution of the axial geometry and spreading rate and direction, *Earth Planet. Sci. Lett.*, *113*, 323–341.
Sloan, H., and P. Patriat (2004a), Reconstruction of the flanks of the Mid-Atlantic Ridge, 28° to 29°N: Implications for evolution of young oceanic lithosphere at slow-spreading centers, *Geochem. Geophys. Geosyst.*, *5*, Q09006, doi:10.1029/2004GC000727.
Sloan, H., and P. Patriat (2004b), Generation of morphotectonic fabric on the Mid-Atlantic Ridge flanks, 28° to 29°N: Implications for the limits of tectonic deformation and abyssal hill formation, *Geochem. Geophys. Geosyst.*, *5*, Q02004, doi:10.1029/2003GC000584.
Smith, D. K., J. R. Cann, and J. Escartin (2006), Widespread active detachment faulting and core complex formation near 13°N on the Mid-Atlantic Ridge, *Nature*, *442*, 440–443.

Tivey, M. A., and B. E. Tucholke (1998), Magnetization of 0-29 Ma ocean crust on the Mid-Atlantic Ridge, 25°30′ to 27°10′N, *J. Geophys. Res.*, *103*, 17,807–17,826, doi:10.1029/98JB01394.

Tivey, M., A. Takeuchi, and WMARK Scientific Party (1998), A submersible study of the western intersection of the Mid-Atlantic Ridge and Kane Fracture Zone (WMARK), *Mar. Geophys. Res.*, *20*, 195–218.

Tucholke, B. E., and J. Lin (1994), A geological model for the structure of ridge segments in slow-spreading ocean crust, *J. Geophys. Res.*, *99*, 11,937–11,958, doi:10.1029/94JB00338.

Tucholke, B. E., J. Lin, and M. C. Kleinrock (1996a), Mullions, megamullions, and metamorphic core complexes on the Mid-Atlantic Ridge, *Eos Trans. AGU*, *77*(46), Fall Meet. Suppl., F724.

Tucholke, B. E., M. C. Kleinrock, and J. Lin (1996b), Cruise Report Ewing 9606 Mid-Atlantic Ridge east flank (MAREAST Survey), 12 July – 17 August 1996, Woods Hole Oceanographic Institution, 71 pp.

Tucholke, B. E., J. Lin, M. C. Kleinrock, M. A. Tivey, T. B. Reed, J. Goff, and G. E. Jaroslow (1997), Segmentation and crustal structure of the western Mid-Atlantic Ridge flank, 25°25′-27°10′N and 0-29 m.y., *J. Geophys. Res.*, *102*, 10,203–10,223, doi:10.1029/96JB03896.

Tucholke, B. E., J. Lin, and M. C. Kleinrock (1998), Megamullions and mullion structure defining oceanic metamorphic core complexes on the Mid-Atlantic Ridge, *J. Geophys. Res.*, *103*, 9857–9866, doi:10.1029/98JB00167.

Tucholke, B. E., K. Fujioka, T. Ishihara, G. Hirth, and M. Kinoshita (2001), Submersible study of an oceanic megamullion in the central North Atlantic, *J. Geophys. Res.*, *106*, 16,145–16,161, doi:10.1029/2001JB000373.

Tucholke, B. E., M. D. Behn, R. Buck, and J. Lin (2008), The role of melt supply in oceanic detachment faulting and formation of megamullions, *Geology*, *36*, 455–458, doi:10.1130/G24639A.

Turcotte, D. L., and G. Schubert (2002), *Geodynamics*, 2nd ed., 472 pp., Cambridge Univ. Press, Cambridge, U. K.

Wang, T., J. Lin, B. E. Tucholke, and Y. J. Chen (2011), Crustal thickness anomalies in the North Atlantic Ocean basin from gravity analysis, *Geochem. Geophys. Geosyst.*, *12*, Q0AE02, doi:10.1029/2010GC003402.

Wessel, P., and W. H. F. Smith (1998), New, improved version of Generic Mapping Tools released, *Eos Trans. AGU*, *79*(47), 579, doi:10.1029/98EO00426.

Whitehead, J. A., H. J. B. Dick, and H. Schouten (1984), A mechanism for magmatic accretion under spreading centers, *Nature*, *312*, 146–148.

Zhao, M. H., J. P. Canales, and R. A. Sohn (2012), Three-dimensional seismic structure of a Mid-Atlantic Ridge segment characterized by active detachment faulting (Trans-Atlantic Geotraverse, 25°55′N-26°20′N), *Geochem. Geophys. Geosyst.*, *13*, Q0AG13, doi:10.1029/2012GC004454.